ISL1 is an essential determinant of structural and functional tonotopic representation of sound

Authors: Iva Filova[a, 1], Kateryna Pysanenko[b,1], Mitra Tavakoli[a], Simona Vochyanova[a], Martina Dvorakova[a], Romana Bohuslavova[a], Ondrej Smolik[a], Sarka Benesova[c], Lukas Valihrach[c], Ebenezer N. Yamoah[d], Josef Syka[b,2], Bernd Fritzsch[e,2], and Gabriela Pavlinkova[a,2,*]

Affiliations:
[a]Laboratory of Molecular Pathogenetics, Institute of Biotechnology CAS, 25250 Vestec, Czechia
[b]Department of Auditory Neuroscience, Institute of Experimental Medicine CAS, 142 20 Prague, Czechia
[c]Laboratory of Gene Expression, Institute of Biotechnology CAS, 25250 Vestec, Czechia
[d]Department of Physiology, School of Medicine, University of Nevada Reno, NV 89557, USA
[e]Department of Biology, Department of Otolaryngology, University of Iowa, Iowa City, IA 52242-1324, USA
[1]I.F. and K.P. contributed equally to this work.
[2]contributed to the conceptualization, evaluation, and writing of this report.
[*]to whom correspondence should be addressed.
Email: Gabriela.Pavlinkova@ibt.cas.cz

Abstract

A cardinal feature of the auditory pathway is frequency selectivity, represented in the form of a tonotopic map from the cochlea to the cortex. The molecular determinants of the auditory frequency map are unknown. Here, we discovered that the transcription factor ISL1 regulates molecular and cellular features of auditory neurons, including the formation of the spiral ganglion, and peripheral and central processes that shape the tonotopic representation of the auditory map. We selectively knocked out *Isl1* in auditory neurons using *Neurod1*^{Cre} strategies. In the absence of *Isl1*, spiral ganglion neurons migrate into the central cochlea and beyond, and the cochlear wiring is profoundly reduced and disrupted. The central axons of *Isl1* mutants lose their topographic projections and segregation at the cochlear nucleus. Transcriptome analysis of spiral ganglion neurons shows that *Isl1* regulates neurogenesis, axonogenesis, migration, neurotransmission-related machinery, and synaptic communication patterns. We show that peripheral disorganization in the cochlea affects the physiological properties of hearing in the midbrain and auditory behavior. Surprisingly, auditory processing features are preserved despite the significant hearing impairment, revealing central auditory pathway resilience and plasticity in *Isl1* mutant mice. Mutant mice have a reduced acoustic startle reflex, altered prepulse inhibition, and characteristics of compensatory neural hyperactivity centrally. Our findings show that ISL1 is one of the obligatory factors required to sculpt auditory structural and functional tonotopic maps. Still, upon *Isl1* deletion, the ensuing central compensatory plasticity of the auditory pathway does not suffice to overcome developmentally induced peripheral dysfunction of the cochlea.

Keywords

spiral ganglion neurons, inferior colliculus, auditory nuclei, inner ear, brain plasticity, *Isl1* mutation, auditory maps, auditory behavior

Introduction

Spiral ganglion neurons (SGNs) are bipolar, extending peripheral processes to the hair cells within the sensory epithelium (the organ of Corti) and central axons towards the cochlear nucleus (CN) complex, the first auditory nuclei in the brain. Sound-induced vibrations that reach the cochlea are amplified by the outer hair cells (OHCs) organized in three rows and innervated by type II SGNs. The inner hair cells (IHCs) receive, transduce, and transmit the auditory signal to type I SGNs that convey the signal via the vestibulocochlear cranial nerve to the CN of the brainstem. The auditory neurons are organized within the cochlea in an orderly fashion according to the frequency with high frequencies at the base and low frequencies at the apex [1, 2]. The cochleotopic or tonotopic pattern is maintained throughout the auditory pathways in the brain [3]. The central auditory pathway transmits ascending acoustic information from the CN through the lateral lemniscus complex, the inferior colliculus in the midbrain, the medial geniculate nucleus of the thalamus to the auditory cortex [4]. The efferent motor neurons consist of the medial olivocochlear motor neurons, which modulate the cochlear sound amplification by OHCs, whereas lateral olivocochlear motor neurons innervate afferent sensory neurons and regulate cochlear nerve excitability [4, 5, 6].

The cellular and molecular regulation of neuronal migration and the establishment of tonotopic connections to the hair cells or neurons of the hindbrain's first auditory nuclei, the CN, are not fully understood. Several transcription factors govern the development of inner ear neurons, including NEUROG1[7], NEUROD1 [8], GATA3 [9, 10], and POU4F1 [11]. However, how the transcriptional networks regulate SGN development and how abnormalities in auditory neurons and neuronal wiring reshape the auditory central pathways' assembly and acoustic information processing remain unresolved.

The transcription factor *Neurod1* plays a vital role in the differentiation and survival of inner ear neurons [12, 13]. We previously demonstrated that *Isl1*^{Cre}-mediated *Neurod1* deletion (*Neurod1CKO*) resulted in a disorganized cochleotopic projection from SGNs [14], affecting acoustic information processing in the central auditory system of adult mice at the physiological and behavioral levels [15]. During ear development, ISL1 is expressed in the differentiating neurons and sensory precursors [14, 16, 17, 18, 19]. *Isl1* is expressed in all four populations of SGNs (type Ia, Ib, Ic, and type II) identified by single-cell RNA sequencing [20]. Studies suggest that ISL1 plays a role in developing neurons and sensory cells, but a direct evaluation of ISL1 inner ear functions remains unknown. Using *Neurod1*^{Cre} [21], we generated a mutant with a conditional deletion of *Isl1* (*Isl1CKO*), eliminating *Isl1* in neurons without directly affecting the development of the inner ear sensory epithelium. We first provide genetic and functional evidence for ISL1's role in establishing spiral ganglion peripheral projection map and proper central auditory circuitry. Most *Isl1CKO* neurons migrated into the center of the cochlear modiolus. They extended outside the cartilaginous otic capsule, in contrast, to control animals with the arrangement of SGNs in parallel to the spiraling cochlear duct. Additionally, we analyzed a transcriptome of neurons, hearing function, sound information processing in the inferior colliculus, and auditory behavior of *Isl1CKO* to demonstrate how the abnormal development of SGNs affects the formation, wiring, and operation of the auditory sensory maps.

Results

The absence of ISL1 causes disorganized innervation and abnormal location of neurons in the cochlea

To investigate the role of ISL1 in inner ear neuron development, we eliminated *Isl1* by crossing *Isl1*$^{loxP/loxP}$ mice [22] with *Neurod1*^{Cre} mice [21]. *Neurod1*^{Cre} is expressed in sensory neurons but not in the sensory epithelium, as visualized by *tdTomato* reporter expression (Additional file 1:

Fig. S1). Analyses of ISL1 expression in *Isl1CKO* confirmed efficient recombination by *Neurod1*^{Cre} with virtually no expression of ISL1 already during the differentiation of neurons in the inner ear ganglion as early as embryonic day E10.5, and later in the cochlear neurons (Additional file 1: Fig. S2). It is worth mentioning that no difference was observed in the density of Schwann cells between the spiral ganglia of *Isl1CKO* and control mice (Additional file 1: Fig. S2C', D').

The overall organization of sensory epithelium in the organ of Corti of *Isl1CKO* was comparable to controls with three rows of OHCs and one row of IHCs (Fig. 1A-E'), as shown by immunolabeling with a hair cell differentiation marker, Myo7a. Whole-mount anti-tubulin staining of innervation showed reduced and disorganized radial fibers. More significant gaps were found between radial fiber bundles, crisscrossing fibers, and unusual dense innervation in the apex, with some large fiber bundles bypassing the organ of Corti and extending to the lateral wall in the *Isl1CKO* cochlea (arrowhead in Fig. 1E'). Note, efferent fibers did not correctly form an intraganglionic spiral bundle (IGSB) in *Isl1CKO.*

Next, we evaluated the effects of *Isl1* deletion on the formation of the spiral ganglion. In control animals, the ganglion was arranged in a spiral parallel to the cochlear duct in the basal and apical half of the cochlea (Fig. 1F, G). In contrast, several SGNs in *Isl1CKO* accumulated beyond the Rosenthal's canal in the center of the basal turn, in the modiolus (arrowhead in Fig. 1H) that usually carries only afferent and efferent fibers. Only a few clusters of neurons were found in the apex (Fig. 1I). The unusual accumulation of cochlear neurons intertwined with the central axons in the modiolus of *Isl1CKO* compared to the control mice is depicted in the immunolabeled sections of the cochlea (Fig. 1J, K). A significantly smaller proportion of neurons located in the regular position parallel to the organ of Corti in the Rosental's canal of *Isl1CKO* compared to the strip of SGNs in the control cochlea (Fig. 1L). In line with the unusual position of SGNs in the *Isl1CKO* cochlea, much elongated and disorganized radial fibers extended from the modiolus to the organ of Corti compared to the control cochlea. Note, efferent bundles of IGSB crossing the radial fibers towards IHCs in *Isl1CKO* (arrows in Fig. 1H). The radial fibers were significantly lengthened in all sections of the *Isl1CKO* cochlea (the apex, mid-apex, mid-base, and base; Additional file 1: Fig. S3), but overall radial fiber density was reduced (Fig. 1M). Anti-tubulin labeling revealed reduced and disorganized innervation in the region of OHCs in *Isl1CKO* compared to controls (Fig. 1N-Q). In controls, fibers extending through the tunnel of Corti were oriented towards the base to form three parallel outer spiral bundles (arrows in Fig. 1N). In contrast, guiding defects in the extension of these fibers in *Isl1CKO* were obvious with neurites extending with random turns towards the base and the apex (Fig. 1P, Q).

Interestingly, *Isl1* deficiency resulted in the shortening of the cochlea that was on average about 20% shorter at postnatal day P0 (Fig. 2A-C). Since *Neurod1*^{Cre} is expressed only in the neurons (Additional file 1: Fig. S1), the shortening of the cochlea appears to be a secondary effect of the abnormalities in neuronal development. A similar phenotype of the truncated growth of the cochlea was reported for *Neurod1* and *Neurog1* mutants because of alternations in spatiotemporal gene expression [7, 14, 15, 23]. Correspondingly to truncated cochlear phenotype [7, 14, 15, 23], detailed analyses showed abnormalities in the epithelium at the apical end with disorganized rows of OHCs and ectopic IHCs among OHCs in the *Isl1CKO* cochlea (Fig. 2D-G).

Altogether, these results demonstrate the prominent effects of *Isl1* deletion on the formation of the spiral ganglion and innervation patterns in the cochlea, and a confounding feature of the truncated cochlea *Isl1CKO* indicates an altered spatial base-to-apex organization of structural and physiological characteristics of auditory neurons.

147

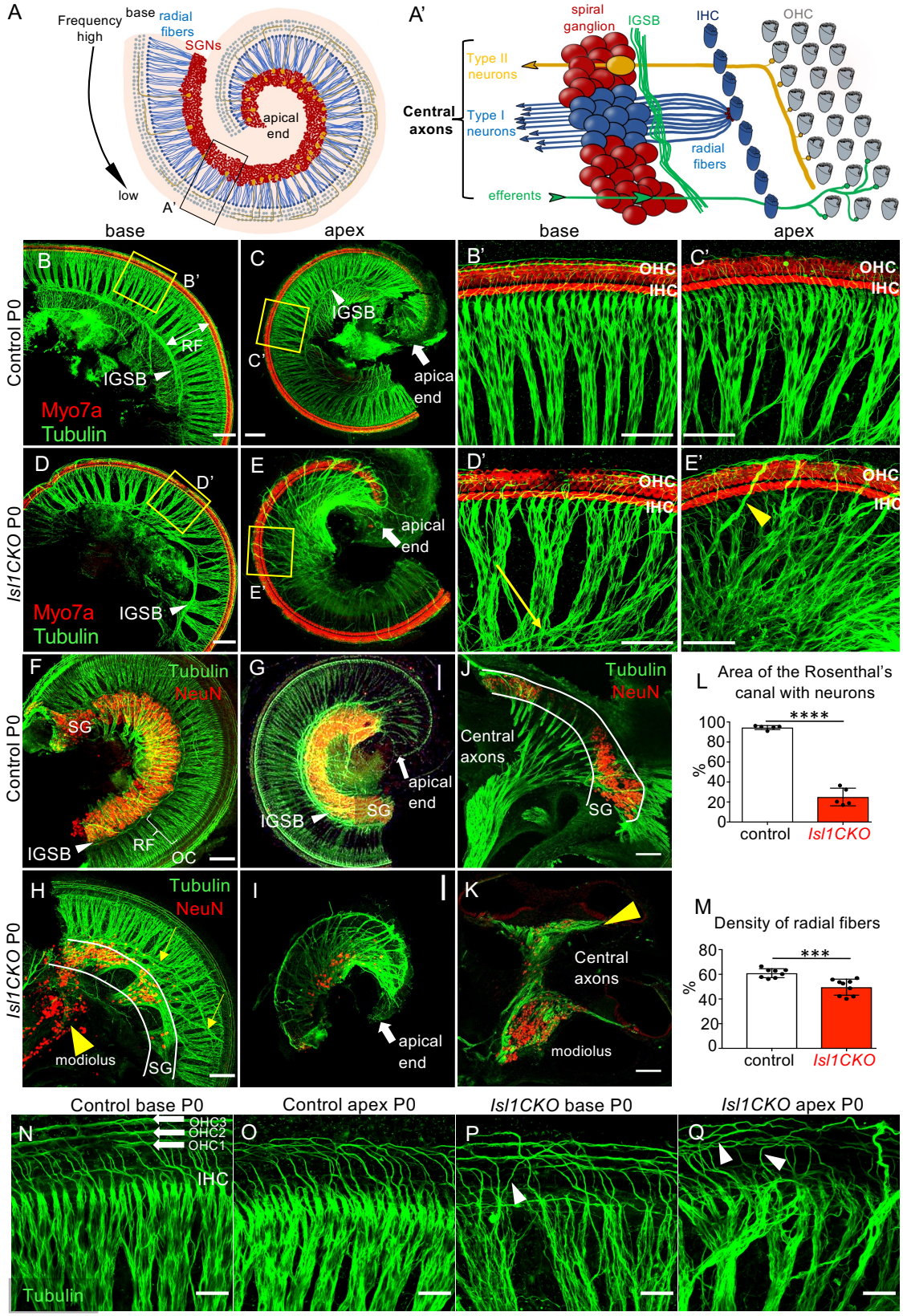

Figure 1. *Isl1* deletion results in abnormalities in cochlear innervation and the formation of the spiral ganglion. (**A**) Diagram of the organization of the cochlea. Spiral ganglion neurons (SGNs) are organized tonotopically from the apex to the base of the cochlea. High-frequency sounds maximally stimulate the base of the cochlea, whereas the largest response to low-frequency sounds occurs in the cochlear apex. (A') The top view diagram onto the sensory epithelium shows outer hair cells (OHCs), inner hair cells (IHCs), and spiral ganglion. Type I neurons extend radial fibers toward IHCs (5-30 neurons innervate one IHC), and type II neurons (representing 5% of SGNs) receive input from OHCs. The central processes of SGNs relay acoustic information to the brain. *(Continued)*

Figure 1 *continued*
Efferent axons from the superior olivary complex, forming the intraganglionic spiral bundle (IGSB), innervate OHCs. (**B-E**) Representative images of whole-mount immunolabeling of the cochlear base and apex with anti-Myo7a (a marker of hair cells) and anti-tubulin (nerve fibers) show reduced and disorganized radial fibers (RF), and missing or altered efferent fibers forming IGSB (arrowhead) in *Isl1CKO* compared to control at postnatal day P0. (**B'-E'**) Higher-magnification images show three rows of OHCs and a row of IHCs forming the organ of Corti and connected to SGNs by RF. Abnormalities in innervation, including larger gaps between radial fiber bundles, crisscrossing fibers (arrows), and fiber bundles bypassing the organ of Corti (arrowheads in E'), are noticeable in the *Isl1CKO* cochlea. (**F-I**) The shape of the spiral ganglion (SG) is shown in the split basal and apical half of the cochlea in whole-mount immunolabeling with anti-NeuN (a nuclear marker of differentiated neurons) and with anti-tubulin (nerve fibers). In controls, anti-NeuN labeled neurons form a spiral parallel to the organ of Corti (OC) with central axons and RF at P0. In contrast, only a small portion of $NeuN^+$ neurons are located in the Rosenthal's canal parallel to the OC in *Isl1CKO* (delineated by white lines in H). The majority of $NeuN^+$ neurons is located in the modiolus (arrowhead). The apical half of the *Isl1CKO* cochlea contains only clusters of neurons (I). Note disorganized IGSB with fiber bundles directly reaching hair cells (arrows in H) and missing IGSB formation in the apex (I). (**J, K**) The vibratome sections of the cochlea labeled with anti-tubulin and anti-NeuN show the unusual position of cochlear neurons in the modiolus and neurons entangled in central axons in *Isl1CKO* compared to control (arrowhead indicates a normal position of the SG). (**L**) Relative comparison of the area of the spiral ganglion in the Rosenthal's canal containing neurons between control and *Isl1CKO*. The values represent mean ± SD (controls n = 5; *Isl1CKO* n = 5); *t*-test ****P < 0.0001. (**M**) The density of radial fibers in the base, mid-base, and mid-apex were lower in the *Isl1CKO* than in the control cochlea. The values represent mean ± SD (n = 3 cochlea per genotype); *t*-test ****P < 0.0001. (**N-Q**) Higher-magnification images show a detail of anti-tubulin labeled innervation with fibers forming three parallel outer spiral bundles (arrows) that innervate multiple OHCs and turning toward the base in the control cochlea. Guiding defects in the extension of these fibers to OHCs are obvious in *Isl1CKO* with some fibers randomly turned toward the apex (arrowheads); note, the disorganization of radial fiber bundles in *Isl1CKO*. Scale bars: 100 μm (B-K), 50 μm (B'-E'), 20 μm (N-Q).

Isl1 regulates neuronal identity and differentiation programs of SGNs

To gain insight at the molecular level about how the *Isl1* elimination causes the neuronal phenotype in the cochlea, we sought to identify potential ISL1 targets through global transcriptome analysis. We opted to use Bulk-RNA sequencing to obtain sequencing depth and high-quality data [24]. Six biological replicates were used per each genotype, and each replicate contained a total of 100 tdTomato positive SGNs isolated from the cochlea embryonic age E14.5. Spiral ganglia were dissected, dissociated into single cells, and fluorescent $tdTomato^+$ cells were FACS-sorted (Fig. 3A). Compared to controls, 650 protein-coding genes were differentially expressed in *Isl1CKO* neurons (adjusted p-value < 0.05, and fold change > 2 cut-off values, see Methods), 332 genes down- and 318 genes up-regulated (Fig. 3B, Additional file 2: Table S1). Gene ontology (GO) term enrichment analysis for the GO term category biological process revealed highly enriched GO terms associated with neuron development, including neurogenesis, neuron differentiation, and nervous system development, in both up- and down-differentially expressed genes (Fig. 3C, Additional file 2: Table S2, S3). The most enriched and specific GO categories for downregulated genes were associated with neurotransmission-related machinery, such as transmembrane transporter, voltage-gated channel, cation and ion transport, and membrane potential regulation, indicating changes in neuronal cell functions. The analysis identified enrichment of downregulated genes involved in axon development, guidance, axonogenesis, and neuronal migration. These genes included members of all four different classes of axon guidance molecules and their cognate receptors, the ephrins-Eph, semaphorins-plexin, netrin-unc5, and slit-roundabout [25], for instance, *Epha5, Epha4, Pdzrn3, Sema3e, Sema6d, Plxna4, Ntn3, Ntng1, Ntng2, Kirrel3, Unc5b, Unc5c, Slitrk3,* and *Slitrk1*. The neurotrophic tyrosine kinase receptors (*Ntrk2* and *Ntrk3*) and a G-protein-coupled chemokine receptor (*Cxcr4*), important regulators of neuronal migration, were also downregulated [26]. These molecular differences dovetail well with abnormalities in the innervation pattern and SGN migration defects in the *Isl1CKO* cochlea. In contrast, upregulated genes particularly enriched in *Isl1CKO* neurons were associated with “regulation of synapse

organization, synapse structure or activity" as well as "regulation of synapse assembly", arguing for compensation of dramatic changes in the ability of neurons to form neuronal projections towards their targets. Upregulated genes encoding molecules critical for synapse formation and adhesion included several members of the cadherin superfamily (*Cdh7, Cdh10*, *Pcdh8, Pcdh9, Pcdh10, Pcdh18,* and *Pcdh19*), adhesion-related genes (*Ptprd, Ptprs, Cntnap2, Itga4, Itga5*), and the ephrin ligands (*Efna3*, *Efna5*). Interestingly, "synaptic signaling" was among GO terms with the significant representation in both up- and down-regulated genes, suggesting changes in synaptic circuits and neuronal activity. We also found many genes encoding transcription factors and signaling molecules, indicating that ISL1 may act through transcription networks instead of defined target genes. The expression of neural-specific bHLH factors important for differentiation and maturation of neurons was increased in *Isl1CKO*, including members of NeuroD (*Neurod6, Neurod2*), Nscl (*Nhlh2*), and Olig (*Bhlhe23*) families [27]. The increased expression of genes encoding LIM domain proteins, the transcription factors *Lhx1, Lhx2*, *Lmo2*, *Lmo*3, and a core member of the PCP signaling paradigm, *Prickle1*, was detected in *Isl1CKO* neurons. *Prickle1* is an important regulator of neuron migration and neurons' distal and central projections in the cochlea [28]. Some of the identified genes encoding regulatory molecules that were shown to be essential for neuronal development, the formation of SGNs, and their projections were downregulated in *ISL1CKO* neurons, such as signaling molecules *Shh* [29], *Wnt3* [30], and *Fgfs* (*Fgf10, Fgf11,* and *Fgf13*)[31, 32], and the transcription factors *Gata3* [9, 10], *Irx1*, *Irx2*, *Pou3f2*, *Pou4f2* [18], and *Runx1* [20, 30]. Selected differentially expressed genes from the RNAseq analysis, namely *Lhx1, Lhx2, Cdh7, Nhlh2, Ntrk2,* and *Ntrk3,* were further validated by RT-qPCR of RNA isolated from whole inner ears of E14.5 embryos (Additional file 1: Fig. S4).

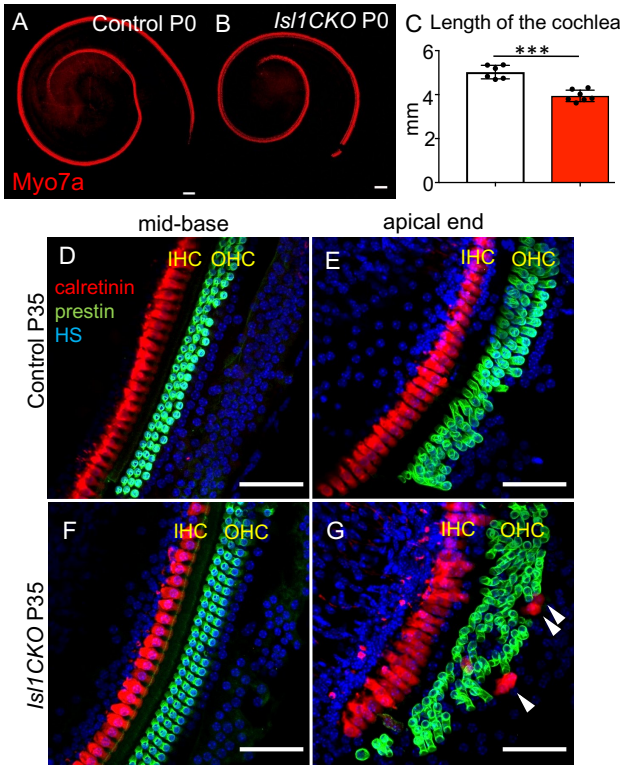

Figure 2. The length of the organ of Corti is shortened in *Isl1CKO*. (**A-C**) The organ of Corti of *Isl1CKO* is 20 % shorter than control at P0, as shown by anti-Myo7a labeling of hair cells. The values represent mean ± SEM (controls 5.0 ± 0.1 mm, n = 6; *Isl1CKO* 3.9 ± 0.1 mm, n = 7); *t*-test ***P < 0.001. (**D-G**) Immunohistochemistry for prestin (a marker for OHCs) and calretinin (a marker for IHCs) shows a comparable cytoarchitecture of the organ of Corti in the cochlear base of controls and *Isl1CKO* but disorganized rows of OHCs in the apical end with multiple HC rows and ectopic calretinin^{+} IHCs among OHCs cells (arrowheads) in *Isl1CKO* at P36. HS, Hoechst nuclear staining. Scale bars: 100 µm (A, B), 50 µm (D-G).

Altogether, these changes indicate that ISL1 regulates transcriptional networks that underlie neuronal identity and function during differentiation of SGNs and that *Isl1* elimination results in a major impairment in the development, axonogenesis, migration, and molecular characteristics of these neurons.

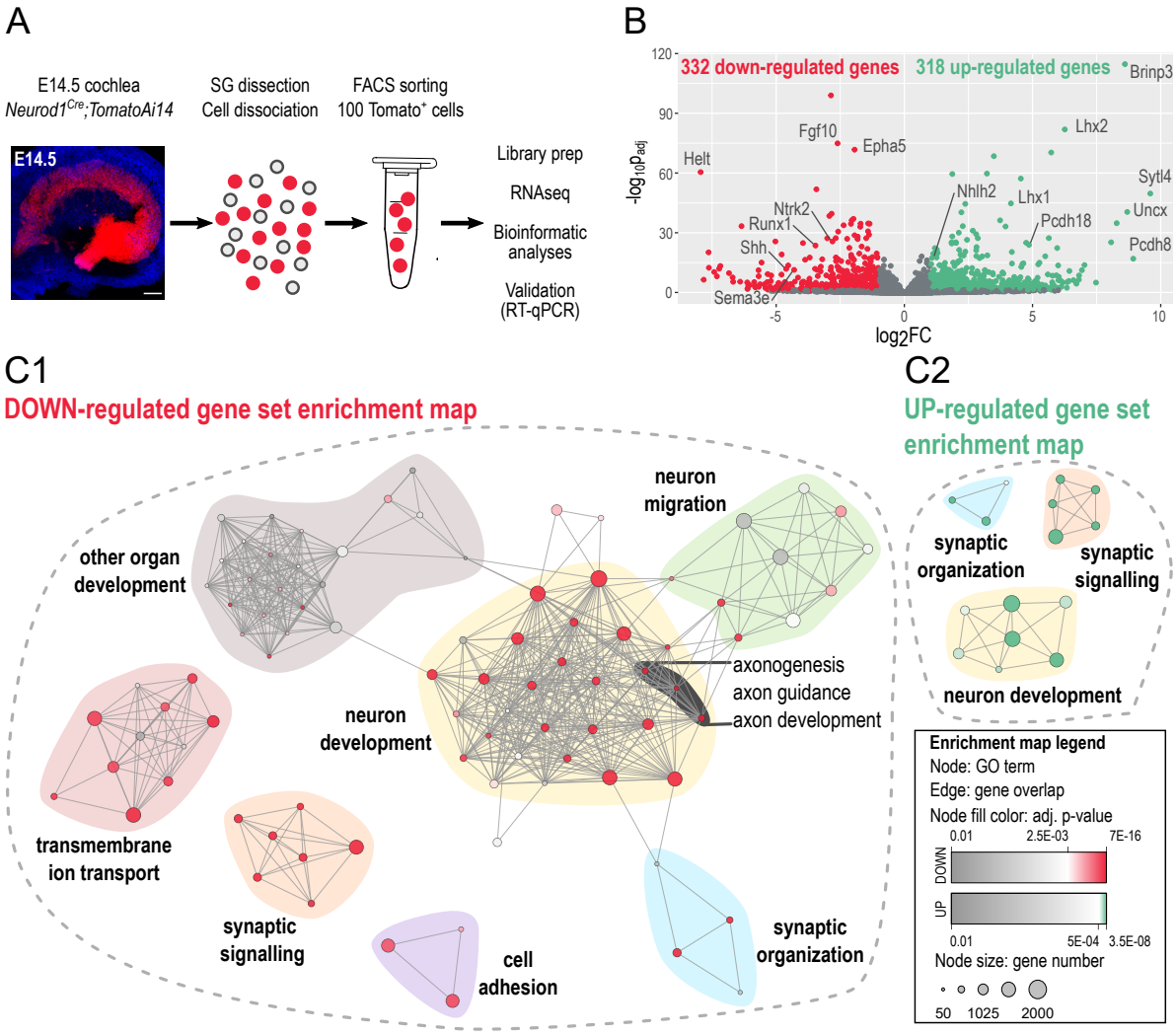

Figure 3. Comparative analysis of control and *Isl1CKO* transcriptomes. (A) Image of the whole-mount cochlea with genetically labeled tdTomato neurons in the spiral ganglion at E14.5 (HS, Hoechst nuclear staining, Scale bar: 100 µm); and workflow depicts microdissection, dissociation, FACS sorting of single tdTomato^{+} spiral ganglion neurons for a bulk of 100 cells RNAseq analysis. **(B)** The volcano plot shows the change in protein-coding genes' expression level in the *Isl1CKO* compared to control spiral ganglion neurons (adjusted p-value < 0.05, and fold change > 2 cutoff values). The complete list of identified 332 down- and 318 up-differentially expressed genes is in Additional file 2, Table S1. **(C)** Enrichment map of down- (C1) and up-regulated (C2) gene ontology (GO) sets visualized by the network. Each node represents a GO term; edges depict shared genes between nodes. Node size represents a number of genes of the mouse genome per the GO term, and node fill color represents a GO term significance. Each GO set cluster was assigned with representative keywords; a list of GO sets is available in Additional file 2, Table S2, S3).

Isl1CKO mice have altered hearing function

Considering the substantial abnormalities in the formation of the spiral ganglion, innervation, and molecular neuron features, we assessed the hearing function of *Isl1CKO* mice. We evaluated distortion product otoacoustic emissions (DPOAE) to determine the robustness of OHC function and cochlear amplification. Otoacoustic emissions are a physiological byproduct of an active amplification mechanism when sound-induced vibrations are amplified in a frequency-specific manner by the OHCs of the organ of Corti [33, 34]. Compared to controls, the DPOAE responses of *Isl1CKO* were significantly reduced in the frequency range between 4 and 24 kHz (Fig. 4A). DPOAE amplitudes at frequencies of 28 kHz and higher were comparable between control and *Isl1CKO* mice. Based on the physiological place-frequency

233

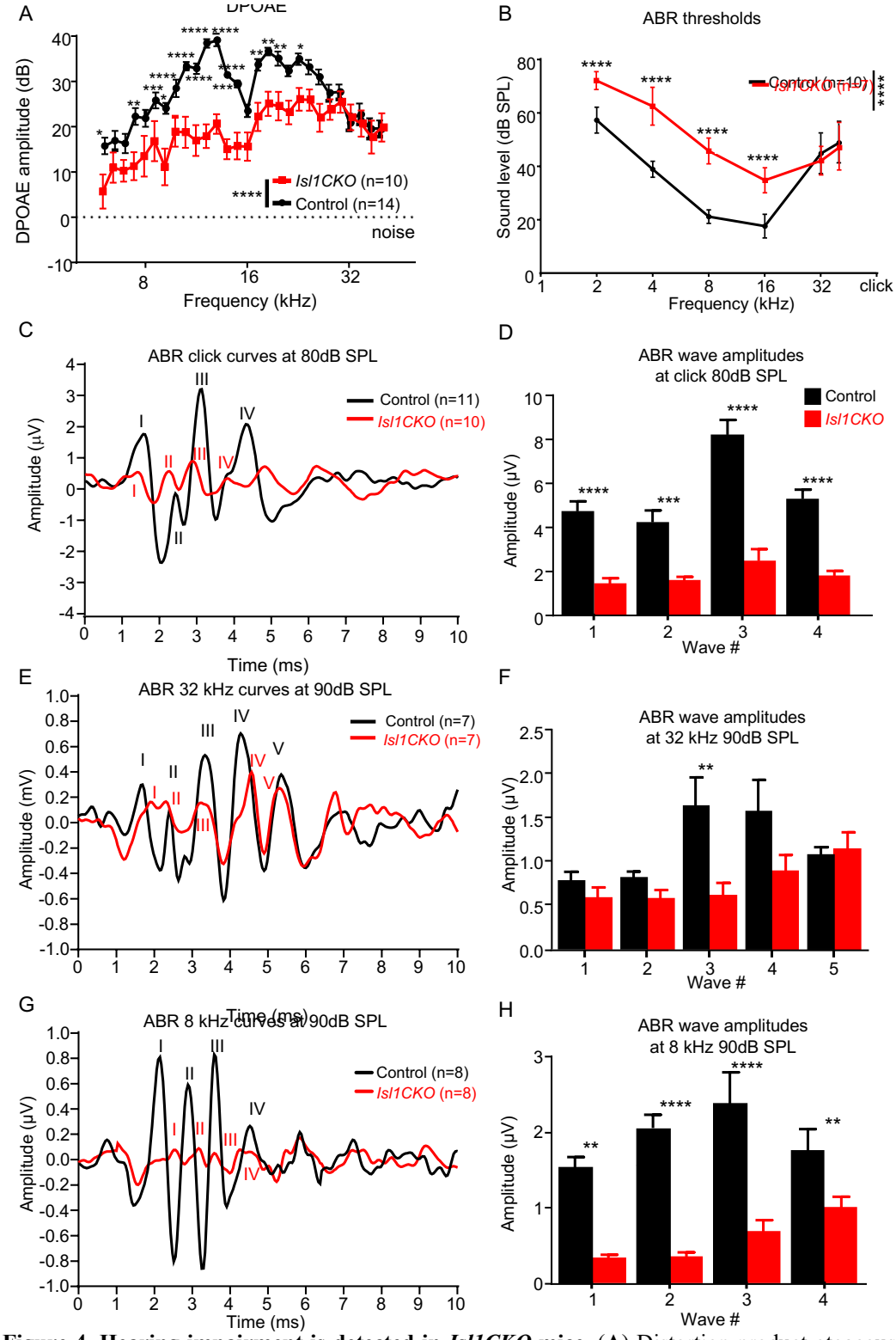

Figure 4. Hearing impairment is detected in *Isl1CKO* mice. (**A**) Distortion product otoacoustic emissions (DPOAEs) show significantly reduced levels in the low and middle-frequency range (6 - 24 kHz). Data are the mean ± SEM, two-way ANOVA with Bonferroni post-hoc test, *P < 0.05, **P < 0.01, ***P < 0.001 ****P < 0.0001. (**B**) The average auditory brainstem response (ABR) thresholds of *Isl1CKO* and control mice are analyzed by click-evoked ABR. Data are the mean ± SD, two-way ANOVA with Bonferroni post-hoc test, ****P < 0.0001. The graphs show averaged ABR response curves evoked (**C**) by an 80 dB SPL click; (**E**) by a 90 dB SPL pure tone of 32 kHz frequency; and (**G**) by a 90 dB SPL pure tone of 8 kHz frequency. (**D, F, H**) Averaged individual ABR wave amplitudes are shown for the corresponding peaks. Data are the mean ± SEM, two-way ANOVA with Bonferroni post-hoc test, **P < 0.01 ***P < 0.001, ****P < 0.0001.

map in the normal mouse cochlea [35], frequencies above 28 kHz are located at the basal half of the cochlea from the mid-base to the basal end. These most preserved DPOAE responses correspond to the most close-to-normal distribution of sensory neurons in the cochlear base in *Isl1CKO* mice (Fig. 1H). Thus, decreased DPOAE responses may be attributed to the overall more profound morphological abnormalities in the apex, including a diminished spiral ganglion, disorganized innervation (Fig. 1E, E', I, Q), and disorganized rows of OHCs in the apical end (Fig. 2G).

We evaluated auditory brainstem responses (ABRs), which measure electrical activity associated with the propagation of acoustic information through auditory nerve fibers. Measurements of ABR thresholds showed that all *Isl1CKO* animals displayed elevated thresholds indicative of hearing loss compared to age-matched control animals, except at frequencies above 32 kHz, which were comparable to ABR thresholds in control mice (Fig. 4B). Using click-evoked ABR, we evaluated waveform characteristics associated with the propagation of acoustic information through the auditory nerve to higher auditory centers (Fig. 4C). Wave I reflects the synchronous firing of the auditory nerve. In contrast, waves II–V are attributed to the electrical activity of downstream circuits in the CN, superior olivary complex, lateral lemniscus, and inferior colliculus [36]. The amplitudes of ABR waves I-IV were significantly reduced in *Isl1CKO* (Fig. 4D). Since the ABR threshold for 32 kHz and above were comparable between age-matched controls and *Isl1CKO* mutants (Fig. 4B), we used the pure-tone stimuli of 32 kHz to evaluate ABR responses (Fig. 4E). A significant difference amongst the genotypes was only found for amplitude reduction of wave III (Fig. 4F), thus indicating preserved synchronized activities of peripheral and brainstem auditory processing. Although waves I and II amplitude for both mutant and control mice were similar, there were apparent differences in the ABR waveform morphology. The latency of ABR wave I was delayed, the relative interwave latency between peaks I and II was shortened, and the trough between wave I and II diminished, resulting in a fusion of both peaks in *Isl1CKO.* A delay of the leading peak of ABR wave I recovered towards ABR wave III. The changes in wave I and II characteristics reflect abnormalities in the summated response from SGNs, auditory nerve fibers, and most likely the CN.

Additionally, we used the pure-tone stimulus of 8 kHz to evaluate ABR responses (Fig. 4G), as ABR thresholds for 8 kHz were significantly reduced for *Isl1CKO* mice. In contrast to the ABR amplitudes at 32 kHz stimuli, the ABR amplitudes for 8 kHz pure-tone stimuli were significantly reduced for all waves (Fig. 4H). The results indicate abnormalities in the cochlear auditory neurons and propagation of acoustic information through auditory nerve fibers to higher auditory centers. We observed a marked drop in the wave I growth function. Still, by comparing wave I and IV peaks, the increased central gain was noted in *Isl1CKO* (Additional file 1: Fig. S5), indicating compensatory plasticity at higher auditory circuits for cochlear damage with diminished afferent input [37].

***Isl1CKO* mice have structural abnormalities in the ascending auditory pathways**

Having recognized the major effects of *Isl1* elimination on the formation of the spiral ganglion and auditory dysfunction, causing sensory hearing loss, as measured by ABRs, we next wanted to establish the morphology of the central auditory pathway components. Using dye tracing, we evaluated the segregation of central axons of the auditory nerve (the cranial nerve VIII; Fig. 5A, schematic view of dye applications). In controls, the central axons labeled by dyes applied into the cochlear base (red) and apex (green) are segregated in the auditory nerve and from the vestibular ganglion, labeled by dye injected into the vestibular end-organs (magenta, Fig. 5B). In contrast, the central axons from the cochlear base (red) and apex (green) virtually overlapped in the auditory nerve (overlapping yellow fibers), and many neurons labeled by the cochlear dye applications were detected to be intermingled with vestibular neurons in *Isl1CKO* (Fig.

284

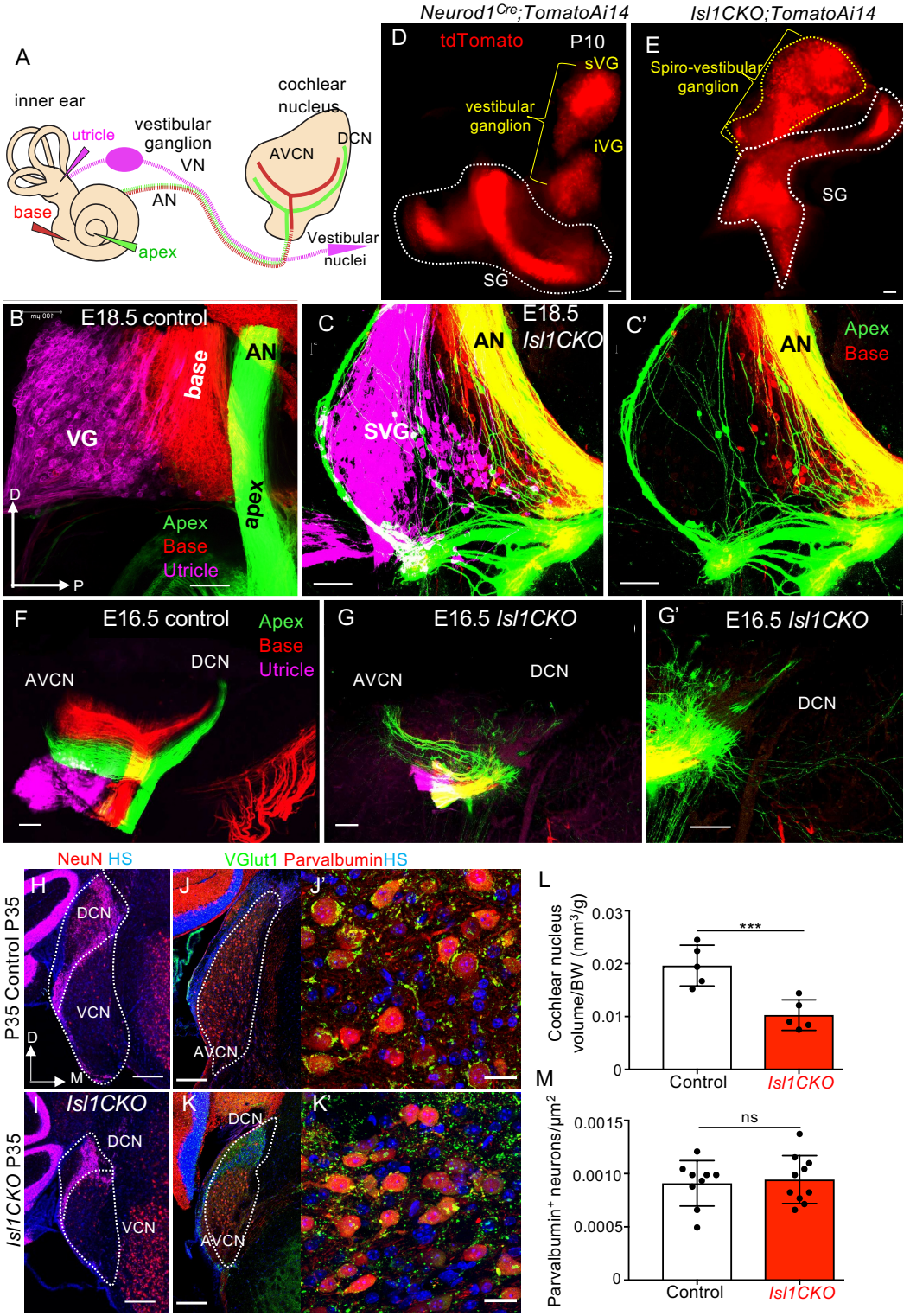

Figure 5. *Isl1CKO* cochlear neurons project unsegregated and disorganized central projections to the cochlear nucleus. (**A**) The schematic diagram visualizes dye tracing from the inner ear and its connections to the auditory brainstem, using insertions of differently colored dyes into the vestibular end organ (the utricle, magenta), cochlear base (red), and cochlear apex (green). Axonal projections from cochlear neurons to the cochlear nucleus (CN) bifurcate with one branch synapsing in the dorsal (DCN) and the other innervating the anteroventral CN (AVCN). **(B-C')** Injections of different colored dyes (magenta into the utricle, red in the base, green in the apex) label distinct and spatially restricted bundles of neuronal fibers (auditory nerve, AN) projecting to the CN and the vestibular ganglion in controls. In contrast, in *Isl1CKO*, the segregation of central axons is lost, as fibers labeled from the apex (green) and base (red) are completely overlapping in the AN (yellow fibers), and neurons labeled by dyes injected into the cochlear base and apex are mixed with vestibular ganglion neurons (magenta) to form an aberrant enlarged ganglion, the spiro-vestibular ganglion (SVG). A merged image shows apical turn dye and base dye-labeled fibers and soma in the SVG (C'). *(Continued)*

Figure 5 *continued*
Note that fibers labeled from the apex (green) form an unusual fiber loop around the SVG in *Isl1CKO* (C, C'). (**D, E**) Whole-mount of the inner ear with tdTomato reporter labeled neurons shows superior (sVG) and inferior vestibular ganglia (iVG), and the spiral ganglion (SG) in the control reporter mouse. In contrast, vestibular ganglia are fused and enlarged, and the spiral ganglion has lost its spiral shape in *Isl1CKO*, shown at postnatal day P10. (**F-G'**) The tonotopic organization of the CN subdivisions in controls is shown by dye tracing in the AVCN and DCN with low-frequency fibers labeled from the apex (green) and high frequency from the base (red). Projections from the base terminate dorsally to the projections from the apex in the control CN. Central projections of afferents in *Isl1CKO* enter as a single bundle from the apex and base instead of forming separate central projections, with just a few fibers occasionally expanding to the DCN. (**H, I**) Coronal sections of a brain (immunostained with anti-NeuN, red) of adult littermate controls and *Isl1CKO*, showing the DCN and VCN; the dotted line indicates the boundaries of the CN. **(J, K)** Representative images of immunolabeling sections of the brain at P35 using anti-parvalbumin to label the bushy cell soma and anti-VGlut1 to label auditory-nerve endbulbs of Held around the spherical and globular bushy cells. **(J', K')** Higher-magnification images show the distribution of parvalbumin$^+$ neurons and the presence of VGlut1$^+$ auditory nerve synaptic terminals. (**L**) Quantification of the adult CN volume, adjusted to body weight and **(M)** a number of parvalbumin$^+$ cells per µm^2 of the AVCN. Data are the mean ± SD. Two-tailed unpaired *t-test* (***P < 0.001; ns, not significant). D, dorsal; P, posterior; M, medial axis. HS, nuclear staining Hoechst. Scale bars: 100 µm (B-G'); 200 µm (H-K); 20 µm (J', K').

5C), forming an aberrant spiro-vestibular ganglion. A merged image shows only apical and basal dye-labeled neuron somas and fibers located in the spiro-vestibular ganglion of *Isl1CKO* (Fig. 5C'). The unusual fibers labeled by the apical dye application (green) were looping around the vestibular ganglion in *Isl1CKO* (Fig. 5C, C'). The distinctive shape of inner ear ganglia in *Isl1CKO* was also confirmed by the tdTomato reporter (Fig. 5D, E). Superior and inferior vestibular ganglia, and the spiral ganglion, recognizable as a coil of cochlear auditory neurons, were clearly distinguished in the control reporter mouse. In contrast, the vestibular ganglia were fused and enlarged, and the cochlear ganglion lost its spiral shape in *Isl1CKO* (Fig. 5E). Unfortunately, the mixing of spiral and vestibular ganglion neurons in *Isl1CKO* mice precluded a full quantitative assessment.

The CN is the first structure of the ascending auditory pathways, where the auditory nerve fibers project. The auditory nerve bifurcated with one branch, synapsing in the posteroventral (PVCN) and dorsal (DCN) CN and the other innervating the anteroventral CN (AVCN; Fig. 5A). Dye tracing showed segregated projections of apical and basal cochlear afferents forming parallel isofrequency bands in controls (Fig. 5F). In contrast, comparable injections in *Isl1CKO* showed that axonal projections to the CN were reduced, restricted, and disorganized and lacked a clear apex and base projection segregations (Fig. 5G). Only a few fibers can occasionally be seen expanding to the DCN in *Isl1CKO* (Fig. 5G'). These results show that tonotopic organization of both the auditory nerve and the CN is lost in *Isl1CKO,* as the cochlear apex and base projections are not segregated. Since the size and number of neurons in the CN depend on input from the auditory nerve during a critical development period up to P9 [38], we also analyzed the volume of the CN of *Isl1CKO*. The volume of the CN of adult mutants was reduced by approximately 50% compared to controls at postnatal day P35 (Fig. 5H, I, L). As *Isl1* is not expressed in the CN [15], the reduced size is likely a secondary effect associated with reduced afferent input consistent with the impact of neonatal cochlear ablation previously reported [2].

The CN contains a variety of neurons with distinct features. The spherical and globular bushy cells are principal cells that receive large auditory nerve endings, called “endbulbs of Held” and “modified endbulbs,” specialized for precise temporal firing [1, 39]. Using anti-parvalbumin to label bushy cell somata and anti-VGlut1 to label auditory-nerve endbulbs of Held around the spherical and globular bushy cells [40, 41], we demonstrated that auditory afferents of *Isl1CKO* and controls formed comparable clusters of boutons that wrap the somas of their targets. Although the CN of *Isl1CKO* was smaller, the number of parvalbumin$^+$ neurons per µm^2 was similar in the VCN of controls and *Isl1CKO* (Fig. 5J-K', M).

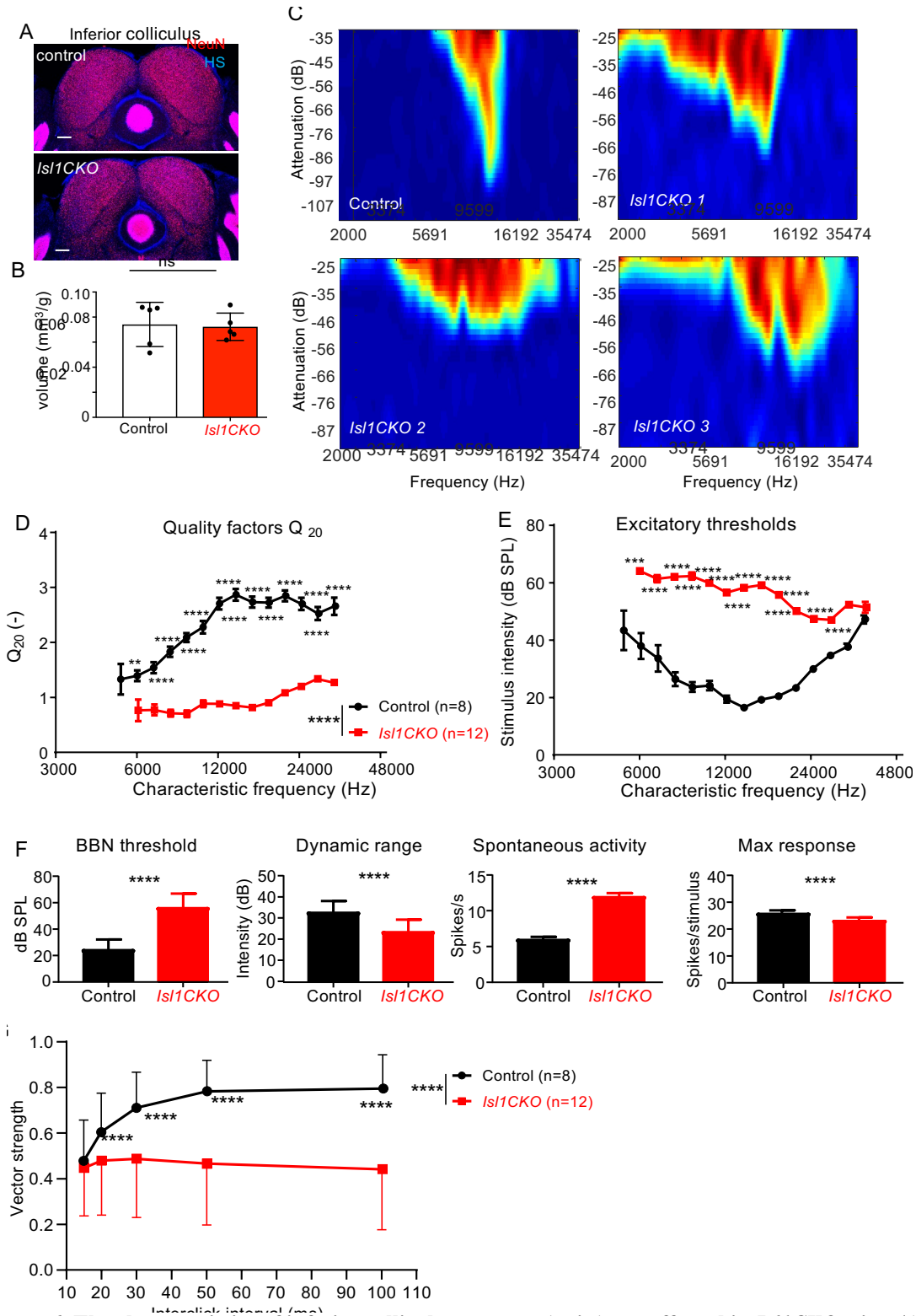

Figure 6. The characteristics of inferior colliculus neurons (units) are affected in *Isl1CKO* mice. (**A**) Immunostaining of coronal brain sections for NeuN and HS, nuclear staining Hoechst, and (**B**) quantification of the volume of the adult control and *Isl1CKO* inferior colliculus (IC; n = 5), adjusted to body weight. Data are the mean ± SD. Two-tailed unpaired *t-test* (ns, not significant). Scale bars, 200 µm. HS, nuclear staining Hoechst (blue). (**C**) Representative examples of tuning curves recorded in the IC display impairments in tuning properties with broad and irregular receptive fields in *Isl1CKO* compared to control mice. (**D**) Excitatory thresholds of the IC neurons at different characteristic frequencies (CF) are shown as averages in 0.3-octave bins in control and *Isl1CKO* mice. (**E**) The sharpness of the neuronal tuning expressed by quality factor Q_{20} (the ratio between the CF and bandwidth at 20 dB above the minimum threshold) averaged in 0.3-octave bins is decreased in *Isl1CKO*. Data are mean ± SEM. Two-way ANOVA with Bonferroni post hoc test. **P < 0.01, ***P < 0.001, ****P < 0.0001. (**F**) Comparison of the rated intensity function parameters between control (n = 8) and *Isl1CKO* (n = 12) mice: broadband noise (BBN) threshold, dynamic range, spontaneous activity, and maximum response magnitude. Data are mean ± SD; unpaired *t*-test, ****P < 0.0001. (**G**) Synchronization of units with click trains. Vector strength computed for different inter-click intervals. Data are the mean ± SD, two-way ANOVA with Bonferroni post-hoc test, ****P < 0.0001.

The tuning properties and excitability of inferior colliculus neurons are distorted in *Isl1CKO*

Having established neuroanatomical changes in the CN, we next evaluated the inferior colliculus (IC) properties, which is the principal auditory structure of the midbrain for the ascending auditory pathways and descending inputs from the ascending auditory pathways auditory cortex [42]. The IC allows for sound localization, integrates multisensory and non-auditory contributions to hearing, and plays an essential role in generating the startle response. We demonstrated no significant IC size reduction in *Isl1CKO* compared to control mice (Fig. 6A, B). We compared neuronal characteristics in the central nucleus of the IC of *Isl1CKO* and control animals using multichannel electrodes. Extracellular electrophysiological recordings of neuronal activity in controls showed a well-defined narrow single-peaked profile of the excitatory receptive fields. In contrast to primarily wide-receptive fields, we observed two or more peaks in *Isl1CKO* mice (Fig. 6C), suggesting multiple inputs from the lower levels of the auditory system. A commonly used metric unit of auditory tuning is the "quality factor," or Q, defined as the characteristic frequency (CF) divided by the bandwidth, measured at 20 dB above the minimum threshold (Q_{20}). Results revealed a significantly lower quality factor in the mutant mice (Fig. 6D), showing substantially worsened frequency selectivity.

The investigation of the responsiveness of IC units to different sound frequencies revealed higher excitatory thresholds in *Isl1CKO* than in control animals in all measured frequencies except for the highest recorded frequencies above 28 kHz (Fig. 6E). These comparable excitatory thresholds for high frequencies between control and *Isl1CKO* mice are consistent with the ABR measurements. We quantified the activity of IC neurons based on the sound intensity, the neuronal responses to a variable intensity of broadband noise (BBN) bursts were analyzed. Compared to control mice, the IC neuronal responses in *Isl1CKO* had a higher BBN threshold, narrower dynamic range, higher spontaneous activity, and significantly lower maximum response magnitudes (Fig. 6F). The results suggest a functional reduction in sensitivity to sound, audibility, and intensity discrimination, as well as increased excitability of IC neurons in *Isl1CKO* mice.

To evaluate the precise temporal representation of sound into the central auditory system, we performed an acoustic stimulation of the IC units with trains of five clicks with different inter-click intervals from 100 ms up to 15 ms. In control mice, the increasing time interval between the clicks led to a better synchronization of neuronal responses with the individual clicks in the train, implying the precision and reliability of the temporal sound discrimination ability (Fig. 6G). In contrast, the precise temporal decoding in *Isl1CKO* was disrupted, as the synchronization of neuronal responses was significantly lower for the whole range of inter-click intervals. In the case of the *Isl1CKO,* the synchronization level of neuronal responses remains almost constant, suggesting a lack of precise temporal sound processing.

The abnormal development of primary auditory neurons alters the auditory behavior of *Isl1CKO* mice

Next, we evaluated the behavioral responses of *Isl1CKO* mice to sound stimuli. The acoustic startle response (ASR) is usually used as a behavioral readout of hearing status mediated by a brainstem circuit linking cochlear root neurons to spinal motoneurons. The structural basis of the ASR includes cochlear root neurons, neurons of the CN, the nucleus of the lateral lemniscus, the caudal pontine reticular nucleus, spinal interneurons, and spinal motor neurons [43, 44, 45]. Similar to the ABR thresholds, the ASR thresholds of *Isl1CKO* significantly increased for startle tone stimuli of 8 kHz and BBN, but not for the high-frequency startle tones (Fig. 7A). The peak latency of the ASR to the BBN stimulation at the 110 dB SPL intensity was prolonged in *Isl1CKO* compared to control mice (Fig. 7B), indicating a slower reaction to the acoustic stimuli. We found significantly reduced ASR amplitudes for all tested sound stimuli

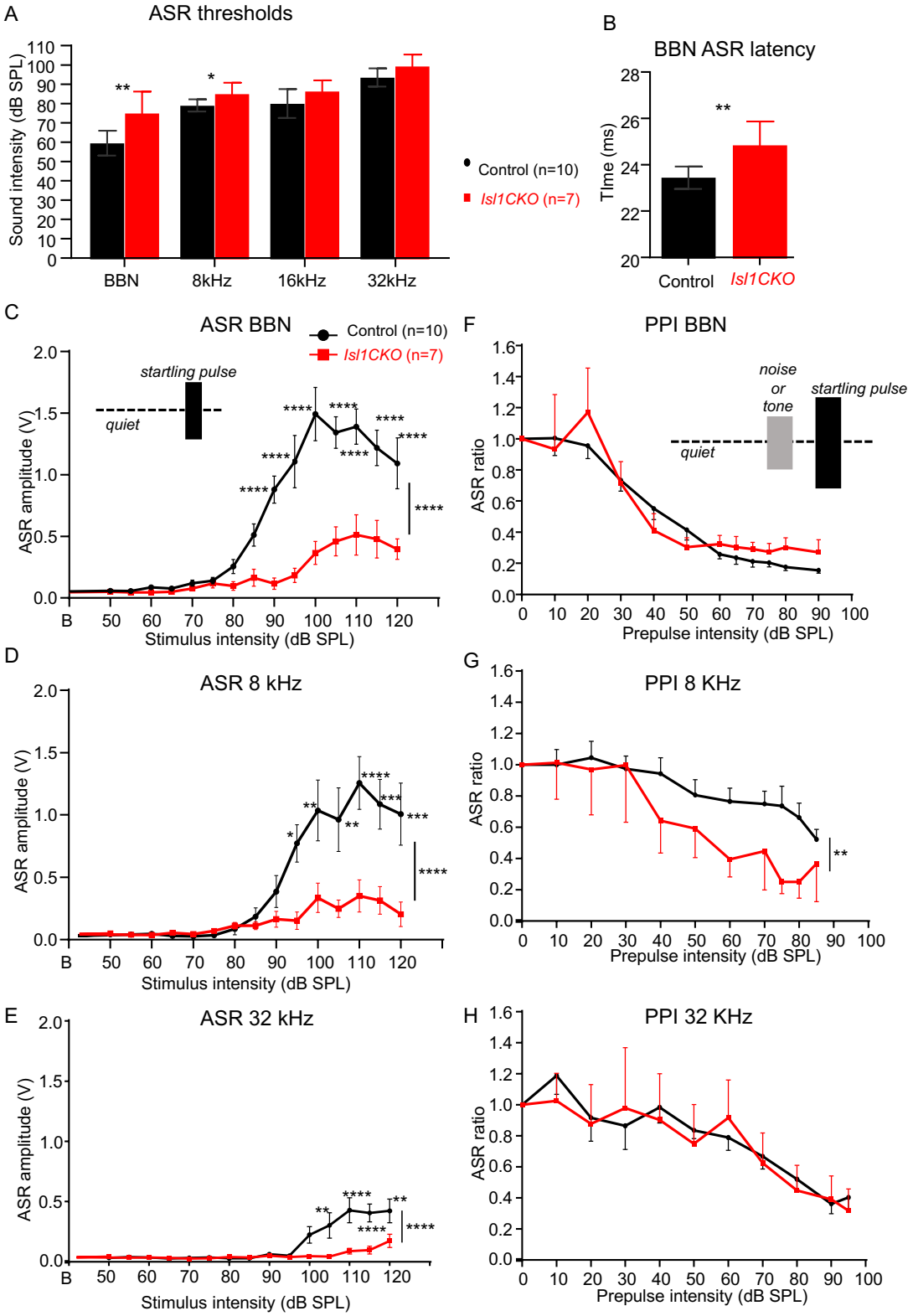

Figure 7. The acoustic startle reflex (ASR) and prepulse inhibition (PPI) responses are altered in the *Isl1CKO* mutant. (**A**) The graph shows the ASR thresholds for broadband noise (BBN) bursts and tone pips at 8, 16, and 32 kHz in control and *Isl1CKO* mice. Data are mean ± SEM. Holm-Sidak method multiple comparison *t*-tests. *P < 0.05, **P < 0.01. (**B**) Significantly increased ASR latency to BBN is found in *Isl1CKO* compared to control mice. Data are mean ± SEM. unpaired *t*-test, **P < 0.01. (**C**) Amplitude-intensity ASR functions for BBN stimulation and (**D**) for tone pips of 8 kHz and (**E**) 32 kHz at different dB SPL intensities in control and *Isl1CKO* mice. (**F**) Efficacy of prepulse intensity on the relative ASR amplitudes was measured the BBN, (**G**) 8 kHz, and (**H**) 32 kHz tone prepulse. ASR ratio = 1 corresponds to the ASR amplitude without a prepulse (the uninhibited ASR). Data are mean ± SEM. Two-way ANOVA with Bonferroni post hoc tests. *P < 0.05, **P < 0.01, ***P < 0.001, ****P < 0.0001.

at higher intensities, showing deteriorated acoustic startle reactivity in *Isl1CKO* mice (Fig. 7C-E).

To further assess complex auditory discrimination behavior, we exposed control and *Isl1CKO* adult mice to a prepulse inhibition (PPI) paradigm, i.e., the inhibition of the ASR induced by presenting an acoustic stimulus shortly preceding the presentation of an acoustic stimulus, the startling sound. The circuit mediating a prepulse on the startle reflex involves central structures of the auditory pathway, including the IC and the auditory cortex [46, 47]. We used either BBN or pure tone pips of 8 and 32 kHz at increasing intensities as a non-startling acoustic stimulus (prepulse) that preceded the startle stimulus in a quiet background. The PPI with the prepulse of a pure tone of 32 kHz, which is the well-preserved audible frequency in *Isl1CKO*, was comparable between control and mutant mice (Fig. 7H). Interestingly, the prepulse with the pure tone of 8 kHz resulted in a larger inhibition of the startle response in *Isl1CKO* than in controls (Fig. 7G), despite the significant hearing deficiency at 8 kHz, as shown by ABR evaluations (Fig. 4). This indicates that the 8-kHz prepulse response was enhanced in *Isl1CKO* mice, suggesting compensatory neural hyperactivity of the central auditory system [37, 48]. Thus, the ASR and PPI of startle analyses indicate abnormalities of the acoustic behavior of *Isl1CKO* mutants.

Discussion

Our study shows for the first time that a LIM homeodomain transcription factor ISL1 regulates neuronal development in the cochlea. Using RNA profiling, morphological, and physiological analyses, we provide evidence that ISL1 coordinates genetic networks affecting molecular characteristics of SGNs, their pathfinding abilities, and auditory information processing. The elimination of *Isl1* in neurons during inner ear development results in migration defect of SGNs, disorganized innervation in the cochlea, unsegregated and reduced central axons, and reduced size of the CN. This neuronal phenotype of *Isl1CKO* was accompanied by hearing impairment, abnormalities in sound processing in the IC, and aberrant auditory behavior.

ISL1 is critical for developing multiple tissues, neuronal and non-neuronal cells [49, 50, 51, 52, 53]. Different aspects of neuronal development depend on ISL1, including specification of motoneurons [49], sensory neurons [22, 51], axonal growth [54], and axonal pathfinding [55]. During inner ear development, ISL1 is expressed in both neuronal and sensory precursors [14, 16, 17, 18, 56]. Transgenic modulations of *Isl1* expression indicate important roles of ISL1 in the maintenance and function of neurons and hair cells and as a possible contributing factor in neurodegeneration [19, 57, 58, 59]. All these studies suggest that ISL1 plays a role in developing neurons and sensory cells, but no direct evaluation of ISL1 function has been performed. To circumvent the pleiotropic effects of *Isl1* in embryonic development, in this study, we used *Neurod1*^{Cre} to delete *Isl1* specifically in the inner ear neurons without affecting the development of sensory cells.

We established that ISL1 is necessary for neuronal differentiation programs in the cochlea and the functional properties of the auditory system. Our RNA profiling of SGNs demonstrated transcriptome changes induced by a loss of *Isl1* affecting molecular characteristics of neurons and pathfinding abilities, including neurotransmission, structure of synapses, neuron migration, axonogenesis, and expression of crucial guidance molecules (neurotrophic tyrosine kinase receptors, *Ntrk2* and *Ntrk3*). Consistent with a central role of ISL1 in sensory neuron developmental programs [22], regulatory networks of signaling molecules and transcription factors were affected in *Isl1CKO* neurons, such as proneural bHLH factors (members of NeuroD, Olig, and Nscl families), LIM-only (*Lmo2*, *Lmo3*) and LIM homeodomain transcription factors (*Lhx1, Lhx2, Isl2*), transcription activation complexes for coordination of particular differentiation programs represented by Eyes absent (*Eya4* and *Eya2*) and Sine oculis (*Six2*) proteins, *Pou3f2* and *Pou4f2* of the family of POU homeodomain

trans-regulatory factors, and FGF signaling molecules (*Fgf10, Fgf11, Fgf13, Fgf14*) and their downstream Etv transcription factor targets (*Etv1, Etv4, Etv5*). Interestingly, transcription factor *Gata3* was downregulated, suggesting that ISL1 is upstream of the Gata3 transcriptional network differentiation program [10]. Thus, ISL1 orchestrates a complex gene regulatory network driving multiple aspects of differentiation of neurons in the cochlea and defining neuronal features.

The most striking morphological features of the neuronal phenotype of *Isl1CKO* are the dysregulated migration and pathfinding of SGNs. A similar migration deficit was reported for *ErbB2* null mutants [60]; however, the interpretation of findings is compounded by direct inner ear effects and effects associated with neural crest-derived Schwann cells. Additionally, conditional deletion of *Sox10* produced by *Wnt1*^{Cre} resulted in abnormal migration of SGNs similar to the *Isl1CKO* phenotype [61]. Migration defects of SGNs in both *ErbB2* [60] and *Sox10* mutants [61] were attributed to the complete absence of Schwann cells in the entire inner ear ganglion. However, in our *Isl1CKO* mutant, SOX10 positive Schwann cells were found in a similar density in the spiral ganglion of both mutant and control mice (Additional File Fig. S2C', D'), thus excluding any direct involvement of glial cells in the migration defects of *Isl1*-deficient neurons. Curiously, more profound disorganization of peripheral processes in the cochlea than defects found in *Isl1CKO* or both *ErbB2* null [60] and *Sox10* mutants [61] was reported for delayed conditional deletion of *Gata3* in SGNs [10]. Despite severe disorganization of cochlear wiring of the *Gata3* conditional deletion mutant, central projections maintained their overall tonotopic organization within the auditory nerve and the CN [9, 10]. In contrast, we provide compelling evidence that elimination of *Isl1* in SGNs affected the pathfinding abilities of neurons in the cochlea not only to form peripheral processes but also to establish central projections. Such profound disorganization of peripheral and central projections is known for *Neurod1* mutations [13, 14, 15]. Deletions of *Neurod1* result in miswired, and reduced SGNs, and loss of tonotopy [13, 15]. Somewhat similar disorganization of central axons with unsegregated auditory nerve fibers, reduced the size of the CN, and missing tonotopic organization of synapsing branches in the CN subdivisions was found in our *Isl1CKO*. Although both *Neurod1CKO* and *Isl1CKO* demonstrated a significant hearing loss, in contrast to the reduced sound frequency range of *Neurod1CKO* [15], responses for the entire measured frequency range were detected in *Isl1CKO*. The processing of high acoustic frequencies was broadly comparable between age-matched controls and *Isl1CKO*, indicating some preservation of peripheral neuronal activity. Accordingly, these most preserved high-frequency basal responses correspond to the most close-to-normal distribution of sensory neurons in the cochlear base in *Isl1CKO* mice (Fig. 1).

Nevertheless, as a result of disorganized primary auditory neurons with derailed central projections, the characteristics of persistent auditory function in the IC were altered with worsened tuning capabilities of IC units and their increased spontaneous activity and threshold elevations and decreased dynamic range. The peripheral deficit in sound encoding results in abnormal auditory behavior of *Isl1CKO*. Although no significant differences of ABR thresholds at 32 kHz were observed between *Isl1CKO* and control mice, indicating retained hearing function, the startle reactions of *Isl1CKO* at 32 kHz were reduced. Plasticity of the startle response is also evident in the PPI responses of *Isl1CKO* mice, in which a weak prestimulus suppresses the response to a subsequent startling stimulus. *Isl1CKO* mice demonstrated PPI impairment for the pure tone of 8 kHz, reflecting abnormal sensorimotor gating due to compensatory hyperactivity of the central auditory system [48, 62].

Additionally, compared to control mice, DPOAE responses of *Isl1CKO* were reduced, indicating dysfunction of cochlear amplification. The OHCs of the organ of Corti play a central role in the active enhancement of sound-induced vibration. For a given OHCs, amplification only occurs at a precise frequency, and thus, this mechanism provides a sharpening of the

tuning curve and improves frequency selectivity [63]. Nevertheless, DPOAE analysis showed that some function was preserved in high-frequency OHCs in the *Isl1CKO* cochlea. Frequencies above 28 kHz are located at the basal half of the mouse cochlea from the mid-base to the basal end [35], which correspond to the most preserved distribution of sensory neurons in the area of the spiral ganglion in the cochlear base of *Isl1CKO* mice (Fig. 1H). Usually, decreased DPOAE amplitudes indicate loss and dysfunction of OHCs [57, 63, 64, 65]. Since *Neurod1*^{Cre} is not expressed in sensory cells in the cochlea, it is unlikely that the development of OHCs is directly affected in *Isl1CKO*. Instead, cochlear amplification deficits in *Isl1CKO* correlated with the reduced and disorganized innervation of OHCs, as shown in Fig. 1. The medial olivocochlear efferents innervate OHCs from the brainstem, representing a sound-evoked negative feedback loop suppressing OHC activity [66]. Besides efferents, OHCs are innervated by the type II SGNs [67, 68]. Although the function of type II SGNs remains obscure, it is clear that these neurons are involved in auditory nociception [69], and may also constitute the sensory drive for the olivocochlear efferent reflex [70] that is disputed [71]. As *Isl1* is expressed in both type I and type II SGNs during inner ear development [20], characteristics of both neuronal types might likely be affected in *Isl1CKO*.

An additional morphological change likely contributing to the hearing deficit of *Isl1CKO* is a shortened cochlea. Somewhat similar phenotypes of a shortened cochlea were previously reported for deletion mutants of *Neurod1* and *Neurog1*, key transcription factors for inner ear neuronal development [8, 14, 15, 72]. A comparable effect of cochlear length reduction was observed following the loss of *Foxg1* [73] and *Lmx1a* [74, 75]. Although mechanisms affecting the cochlear extension are unknown, it is clear that this confounding feature of the *Isl1CKO* phenotype would consequently impact mechanical and neural tuning from the base to the apex of the cochlea and the ability to perform time-frequency processing of sound.

Conclusions

Our study provides compelling evidence that ISL1 is a critical regulator of SGN development, affecting neuronal migration, pathfinding abilities to form cochlear wiring, and central axonal projections. As such, ISL1 represents an essential factor in the regulation of neuronal differentiation to produce functional neurons in cell-based therapies and stem cell engineering [76, 77]. Additionally, this unique model contributes to our understanding of how disorganization of the neuronal periphery affects information processing at higher centers of the central auditory pathway at the physiological and behavioral levels. ISL1 is a LIM-homeodomain transcription factor with a specific potential to interact and recruit other co-factors to form higher-order regulatory complexes [78]. In the future, it will be intriguing to fully identify the molecular mechanisms and co-regulators underlying ISL1 function in SGNs.

Methods

Experimental animals

All methods were performed according to the Guide for the Care and Use of Laboratory Animals (National Research Council. Washington, DC. The National Academies Press, 1996). The design of experiments was approved by the Animal Care and Use Committee of the Institute of Molecular Genetics, Czech Academy of Sciences. The mice were housed in 12-hour light/dark cycles and were fed *ad libitum*. To generate *Isl1CKO* (the genotype *Neurod1*^{Cre}*;Isl1*$^{loxP/loxP}$), we cross-bred floxed *Isl11* (*Isl1*$^{loxP/loxP}$; *Isl1*^{tm2Sev}*/J,* # 028501, Jackson Laboratory)[22] and *Neurod1*^{Cre} transgenic mice (Tg(Neurod1-cre)1Able/J, # 028364, Jackson Laboratory), which were generated by pronuclear injection of the *Neurod1-cre* BAC construct that carries Cre-sequence downstream of the translational initiation codon ATG of the *Neurod1* gene [21]. Heterozygous animals, *Neurod1*^{Cre}*;Isl1*$^{+/loxP}$ were viable, born in appropriate

Mendelian ratios, and were phenotypically indistinguishable from control (Cre negative) littermate mice. As control mice, we used mice with the genotype Cre negative, *Isl1*$^{loxP/loxP}$ and *Isl1*$^{+/loxP}$. The mouse line *Neurod1*^{Cre} was also bred with Cre-reporter tdTomato line (*TomatoAi14*, B6.Cg-*Gt(ROSA)26Sor*$^{tm14(CAG-tdTomato)Hze}$, # 7914 Jackson Laboratory). PCR performed genotyping on tail DNA. We used both males and females for experiments. Lines are a mixed C57BL/6/sv129 background. Phenotyping and data analysis was performed blind to the genotype of the mice.

Morphological evaluation of the cochlea, cochlear nucleus, and inferior colliculus

Dissected ears were fixed in 4% paraformaldehyde (PFA) in PBS. For vibratome sections, samples were embedded in 4% agarose and sectioned at 80 µm using a Leica VT1000S vibratome. Vibratome sections, whole inner ears, or whole embryos were defatted in 70% ethanol and then rehydrated and blocked with serum, as described previously [16, 58]. Samples were then incubated with primary antibodies at 4ºC for 72 hours. The primary antibodies used were: rabbit anti-Myosin 7a (Myo7a; Proteus BioSciences 25-6790, 1:500), mouse anti-acetylated α-tubulin (tubulin; Sigma-Aldrich T6793, 1:400), rabbit anti-calretinin (Santa Cruz Biotechnology sc-50453, 1:100), rabbit anti-parvalbumin (Abcam ab11427, 1:2000), mouse anti-VGLUT1 (Merck MAB5502, 1:200), rabbit anti-NeuN (Abcam ab177487, 1:500), goat anti-prestin (Santa Cruz Biotechnology sc-22692, 1:50), mouse anti-Isl1 (Developmental Hybridoma Bank 39.3F7, 1:130), goat anti-Neurod1 (Santa Cruz Biotechnology sc-1084, 1:100), and rabbit anti-Sox10 (Abcam ab155279, 1:250). After several PBS washes, secondary antibodies were added and incubated at 4ºC for 24 hours. The secondary antibodies Alexa Fluor® 488 AffiniPure Goat Anti-Mouse IgG (Jackson ImmunoResearch Laboratories 115-545-146), Alexa Fluor® 594 AffiniPure Goat Anti-Rabbit IgG (Jackson ImmunoResearch Laboratories 111-585-144), and DyLight488-conjugated AffiniPure Mouse Anti-Goat IgG (Jackson ImmunoResearch Laboratories 205-485-108) were used in 1:400 dilution. Nuclei were stained by Hoechst 33258 (Sigma-Aldrich 861405, 1:2000). Samples were mounted in Aqua-Poly/Mount (Polysciences 18606) or prepared Antifade medium, and images were taken on Zeiss LSM 880 confocal microscope. ImageJ and ZEN software was used for image processing.

The length of the organ of Corti was measured using the "Measure line" ImageJ plugin. The CN and inferior colliculus volumes were established by analyzing parallel, serial equally spaced 80 µm coronal vibratome sections through the brain (n = 5 *Isl1CKO* and n = 5 control mice). The left and right cochlear nucleus and inferior colliculus areas were determined in each section using ImageJ, and the volume of the organs was calculated. Volumes of paired organs were adjusted to the body weight. Whole-mount anti-tubulin labeling of the cochlea was used to measure the length and density of the radial fibers. The evaluation of the innervation was done separately for each part of the cochlea: the apex, mid-apex, mid-base, and base. Due to the disorganization of innervation in the apex, we only evaluated the fiber density in the cochlea's base, mid-base, and mid-apex parts. The density of the radial fibers was expressed as the percentage of a positive area in the measured area of 152 x 66 µm^2 using the “Threshold” function ImageJ. The length of the radial fibers was measured from the whole-mount anti-tubulin and Myo7a immunolabeled cochlea confocal images. For each genotype, we measured 3 samples, and in each part of the cochlea, we measured the length of the fibers in 3 radial fiber bundles from the IHCs to the IGSB. To compare how many neurons are correctly located in the area of the Rosental's canal in *Isl1CKO*, we used NeuN immunolabeled whole-mount cochlea. We measured the corresponding region of the spiral ganglion-containing neurons using the “Threshold” function ImageJ. We used 5 samples per genotype.

Isolation of genetically labeled neurons and library construction

Spiral ganglia were micro-dissected in Dulbecco's PBS on ice from E14.5 embryos of either sex from four litters; spiral ganglia from both inner ears of the individual embryo per sample. Spiral ganglia were incubated in 300 µl of lysis solution (0.05% trypsin, 0.53mM EDTA Dulbecco's PBS) in 37 ºC, shaking at 900 RPM for 5 min. The lysis was stopped by adding 600 µl of FACS buffer (Dulbecco's PBS, 10mM EGTA, and 2% FBS). After spinning down the samples at 800 G, 4 ºC for 10 min, the supernatant was removed, and cell pellets were resuspended in 500 µl of ice-cold FACS buffer. Immediately before sorting, cells were passed through a 50 µm cell sieve (CellTrics™, Sysmex Amercica Inc.) into a sterile 5 ml polystyrene round-bottom falcon to remove clusters of cells and kept on ice. TdTomato^{+} neurons were sorted using a flow cytometer (BD FACSAria™ Fusion), through a 100 µm nozzle in 20 psi, operated with BD FACSDiva™ Software. 100 sorted cells were collected into individual wells of 96-well plate containing 5 µl of lysis buffer of NEB Next single-cell low input RNA library prep kit for Illumina (#E6420 New England Biolabs). Plates were frozen immediately on dry ice and stored at −80 °C. The total time from euthanasia to cell collection was ~3 hrs.

RNAseq-libraries were prepared from 6 samples per each genotype, control (*Neurod1^{Cre}; TomatoAi14*) and *Isl1CKO* mutant (*Isl1CKO;TomatoAi14)*, and each sample contained 100 tdTomato^{+} neurons. Following the manufacturer's instructions, the NEB Next single-cell low input RNA library prep kit for Illumina was used for cDNA synthesis, amplification, and library generation [79] at the Gene Core Facility (Institute of Biotechnology CAS, Czechia). Fragment Analyzer assessed the quality of cDNA libraries. The libraries were sequenced on an Illumina NextSeq 500 next-generation sequencer. NextSeq 500/550 High Output kit 75 cycles (# 200024906, Illumina) were processed at the Genomics and Bioinformatics Core Facility (Institute of Molecular Genetics CAS, Czechia).

Computational analysis of RNAseq data

RNA-Seq reads in FASTQ files were mapped to the mouse genome using STAR [version 2.7.0c [80]] version GRCm38 primary assembly and annotation version M8. The raw data of RNA sequencing were processed with a standard pipeline. Using cutadapt v1.18[81], the number of reads (minimum, 32 million; maximum, 73 million) was trimmed by Illumina sequencing adaptor and of bases with read quality lower than 20, subsequently reads shorter than 20 bp were filtered out. TrimmomaticPE version 0.36 [82]. Ribosomal RNA and reads mapping to UniVec database were filtered out using bowtie v1.2.2. with parameters -S -n 1 and SortMeRNA [83]. A count table was generated by Rsubread v2.0.1 package using default parameters without counting multimapping reads. The raw RNAseq data were deposited at GEO: # GSE182575 study (https://www.ncbi.nlm.nih.gov/geo/query/acc.cgi?acc=GSE182575). DESeq2 [v1.26.0 [84]] default parameters were used to normalize data and compare the different groups. Differentially expressed genes were identified based on an adjusted P-value $p_{adj} < 0.05$, FC > 2, and a base mean ≥ 50 was applied to identify differentially expressed genes between *Isl1CKO* mutant and control neurons. The functional annotation of the differentially expressed genes was performed using GOTermFinder [85].

Enrichment mapping. The enrichment of the functional categories and functional annotation clustering of the differentially expressed genes were performed using g: Profiler [86] input using version e104_eg51_p15_3922dba with g: SCS multiple testing correction methods applying significance threshold of 0.05, while no electronic GO annotations were used. Only Biological Processes (BP) data underwent further processing. Complete query details are available in Query info tabs in Additional Supplementary file 2, Table S2, S3. The resulting GEM and combined GMT files were loaded into Cytoscape [87] plugin "EnrichmentMap" [88] using 0.01 FDR q-value cutoff to generate a network. Edge cutoff was set to 0.6, and nodes were filtered by gs_size<1800. Five GO terms forming solitary nodes, or a pair of nodes, were excluded

(listed in Additional Supplementary file 2, Table S2, S3). Further adjustments were made in yFiles Layout Algorithms, Legend Creator (Cytoscape plugins), and Inkscape (Inkscape Project, 2020).

Quantitative real-time PCR

Total RNA was isolated from both inner ears of the embryo at E14.5 using TRI Reagent (Sigma-Aldrich T9424). We used 8 embryos for *Isl1CKO* and 7 embryos for the control group from three litters. RNA from both inner ears of one embryo represented one sample. RNA samples (1 μg) were processed and analyzed as previously described [58]. Briefly, following RT, quantitative qPCR was performed with initial activation at 95 °C for 120 s, followed by 40 cycles at 95 °C for 15 s, 60 °C for 30 s, and 72 °C for 30 s using the CFX384™ Real-Time PCR Detection System (Bio-Rad Laboratories). The primer sequences (pga.mgh.harvard.edu/primerbank/) are listed in Additional Supplementary file 2, Table S4. Relative mRNA expression was calculated using the –ΔΔCq method with *Hprt1* as a reference gene. GraphPad Prism software was used for statistical analysis.

Lipophilic Dye Tracing

We studied the innervation pattern in whole or dissected ears using lipophilic dye tracing in aldehyde-fixed tissues as previously described [89]. At least three mutants and similar numbers of control littermates of both sexes were used for each evaluation. Filter strips loaded with colored lipophilic dyes were inserted into the cochlear apex, base, and vestibular end-organ utricle [90]. After allowing appropriate time for diffusion of the lipophilic tracer (between 48-120 hours), we prepared the ears as whole mounts in glycerol on a glass slide, using appropriate spacers to avoid distortion, and imaged them using a Leica SP8 confocal microscope. Images were compiled into plates to show the most pertinent details using Corel Draw. Only general image modifications such as contrast or brightness adjustments were used to enhance the visual appeal without affecting the scientific content.

Hearing function evaluation

Auditory brainstem response (ABR) and distortion product otoacoustic emissions (DPOAEs) tests were carried out on mice under general anesthesia with 35 mg/kg ketamine (Calypso 50 mg/ml) and 6 mg/kg xylazine (Xylapan 20 mg/ml) in saline to give an application volume of 7 ml/kg body weight via subcutaneous injection, maintained on a temperature-regulated blanket in a soundproof room.

Distortion product otoacoustic emissions. For DPOAE recording were tested *Isl1CKO* (n = 10) and control mice (n = 14). Cubic (2 F1–F2) distortion product otoacoustic emissions over an F2 frequency range from 6 to 38 kHz were recorded with a low-noise microphone system (Etymotic probe ER-10B+, Etymotic Research). Acoustic stimuli (ratio F2/F1 = 1.21, F1 and F2 primary tone levels of L1/L2 = 70/60 dB) were presented to the ear canal with two custom-made piezoelectric stimulators connected to the probe with 10-cm-long silastic tubes. The signal from the microphone was analyzed by the TDT System III (RP2 processor, sampling rate 100 kHz) using custom-made MATLAB software. DPOAEs were recorded in the animals' ears at individual frequencies over the frequency range 4–38 kHz with a resolution of ten points per octave. All the experiments and analyses were done with no information on the genotype.

Auditory brainstem response. For auditory brainstem response (ABR) recording (n = 7 *Isl1CKO* and n = 10 control mice), an active electrode was placed subcutaneously on the vertex and ground and reference electrodes in the neck muscles. Responses to tone bursts (3 ms duration, 1 ms rise/fall times, frequencies of 2, 4, 8, 16, 32, and 40 kHz) and clicks of different intensity were recorded. Acoustic stimuli were conveyed to the animal in free-field conditions via a two-way loudspeaker system (Selenium 6W4P woofer and RAAL70-20 tweeter) placed

70 cm in front of the animal's head. The signal was processed with a TDT System III Pentusa Base Station and analyzed using BioSig™ software. The response threshold to each frequency was determined as the minimal tone intensity that still evoked a noticeable potential peak in the expected time window of the recorded signal. The amplitude and latency of ABR peaks I-V were determined using BioSig software (Tucker Davis Technologies). Central compensation of neuronal responsiveness (central gain) was calculated using ABR wave IV to I amplitudes.

Extracellular recording of the neuronal activity in the inferior colliculus (IC)

For extracellular recording in the IC, we evaluated *Isl1CKO* (n = 8) and control mice (n = 12). The surgery and extracellular recording in the IC were performed in mice anesthetized with 35 mg/kg ketamine (Calypsol 50 mg/ml) and 6 mg/kg xylazine (Xylapan 20 mg/ml) in saline via subcutaneous injection. Approximately every hour, supplement subcutaneous injections of one-half of the original dose of the anesthetics were administered to keep a sufficient level of anesthesia, judged by a positive pedal and palpebral (toe-pinch) reflex and movement of the whiskers. Respiratory rate, and heart rate, were monitored. An incision was made through the skull's skin for access to the IC, and underlying muscles were retracted to expose the dorsal skull. A holder was glued to the skull, and small holes were drilled over both ICs. Neuronal activity (multiple units) in the IC was recorded using a 16-channel, single shank probe (NeuroNexus Technologies) with 50 or 100 μm between the electrode spots. The obtained signal from the electrode was amplified 10000 times, band-pass filtered over the range of 300 Hz to 10 kHz and processed by a TDT System III (Tucker Davis Technologies) using an RX5-2 Pentusa Base Station. Individual spikes from the recorded signal were isolated online based on amplitude discrimination and analyzed with BrainWare software (v. 8.12, Jan Schnupp, Oxford University). Subsequent discrimination of spikes from the recorded data and their sorting according to the amplitudes of the first positive and negative peaks were performed off-line and was used to sort action potentials (spikes) among single units. The recorded data were processed and analyzed using custom software based on MATLAB. The stimulation signals were generated using a TDT System III with the RP 2.1 Enhanced Real-Time Processor. Acoustic stimuli were delivered in free-field conditions via a two-driver loudspeaker system (Selenium 6W4P woofer and RAAL70-20 tweeter) placed 70 cm in front of the animal's head.

Frequency-intensity mapping: To determine the neuronal receptive fields, pure tones (frequency 2 - 40 kHz with 1/8 octave step, 60 ms duration, 5 ms rise/fall times, various intensity with 5dB step) were presented in a random order, each stimulus appearing three times. A discrete matrix corresponding to the response magnitude evoked by each of the frequency-intensity combinations was thereby obtained, smoothed using cubic spline interpolation, and used for extraction of the basic parameters: the excitatory response threshold (the lowest stimulus intensity that excited the neuron, measured in dB SPL), the characteristic frequency (CF) – the frequency with the minimal response threshold, measured in Hz, and the bandwidth of the excitatory area 20 dB above the excitatory threshold, expressed by quality factor Q (Q = CF/bandwidth).

Rate intensity function of the IC neurons: Neuronal responses to broadband noise (BBN) bursts of variable intensity (10 dB steps, 50 repetitions) were used to construct the rate intensity function (RIF). A 100% scale was assigned to the neuron's total range of response amplitudes, 0% corresponding to spontaneous activity and 100% corresponding to its maximum response magnitude [91]. The two points of interest are R10 and R90, which correspond to 10 and 90% of this scale, respectively. R10, describing the starting point of the RIF's rise, was taken as the BBN response threshold. RIFs were further used for evaluating the following parameters: the dynamic range (DR) of the RIF: DR = S90–S10); and the maximum response magnitude. Spontaneous activity of the IC neurons was determined at the 0dB SPL BBN stimulation.

Temporal properties of the IC neurons: We used trains of five clicks at an intensity of 70 dB SPL for control and 80 dB SPL for *Isl1CKO* mice with various inter-click intervals (100, 50, 30, 20, and 15 ms). We calculated the vector strength (VS) values and the Rayleigh statistics for each spike pattern; only responses with at least 5.991 were significantly considered phase-locking (Zhou and Merzenich, 2008). The VS quantifies how well the individual spikes are synchronized (phase-locked) with a periodic signal.

Behavioral tests

Isl1CKO (n = 10) and control (n = 7) mice were used at 2-3 months of age. All behavioral tests were performed in a sound-attenuated chamber (Coulbourn Habitest, model E10-21) located in a soundproof room. Each mouse was placed in a wire mesh cage on a motion-sensitive platform inside the box during the testing. The mouse's reflex movements to sound stimuli were detected and transformed to a voltage signal by the load-cell response sensing platform. An amplified voltage signal was acquired and processed using a TDT system 3 with a Real-Time Processor RP 2 (Tucker Davis Technologies, Alachua, Fl) and custom-made software in a Matlab environment. The startle responses were evaluated in 100 ms windows, beginning at the onset of the startling stimulus. The magnitude of the response was measured as the maximal peak-to-peak amplitude of transient voltage occurring in the response window. Acoustic stimuli were generated by the TDT system (Real-Time Processor RP 2), amplified and presented via a loudspeaker (SEAS, 29AF/W), and placed inside the chamber above the animal. Stimulus presentation and data acquisition were controlled by a custom-made application in a Matlab environment. Calibration of the apparatus was performed for frequencies between 4 kHz and 32 kHz by a 1/4-inch Brüel & Kjaer 4939 microphone connected to a Brüel & Kjaer ZC 0020 preamplifier and a B&K 2231 sound level meter. During the calibration, the calibrating microphone was positioned at the animal's head in the test cage.

Acoustic startle reflex (ASR) (a transient motor response to an intense, unexpected stimulus) was used to indicate the behavioral responsiveness to sound stimuli**.** The ASRs to 8, 16, and 32 kHz tone pips and BBN bursts (50 ms duration, 3 ms rise/fall times, varying intensity levels) were recorded. Each test session contained: a baseline trial (–10 dB SPL stimulus intensity) and 13 startle stimuli of different intensities (50, 55, 60, 65, 70, 75, 80, 85, 90, 100, 110, 115, and 120-dB SPL). The inter-trial interval varied from 15 to 50 s.

In *the prepulse inhibition (PPI)* procedure, 3 different trial types were used: a baseline trial without any stimulus, an acoustic startle pulse alone (white noise at 110 dB SPL, 50 ms, 3 ms rise/fall times), and a combination of the prepulse and startle pulse. The inter-stimulus interval between the prepulse and the startle stimulus was set to 50 ms; each trial type was presented three times. The inter-trial gap was randomized and varied from 15 to 50 s. The efficacy of the PPI of ASR was expressed as an ASR ratio in percentage, e.g., 100% corresponds to the amplitude of ASR without prepulse; smaller values of ASR ratio indicate stronger PPI. As a prepulse, we used either BBN bursts or tone pips (50 ms duration, 3 ms rise/fall time) at frequencies of 8 and 32 kHz at increasing intensities. It is expected that in the presence of prepulse, the amplitude of the following startle response decreases.

Experimental design and statistical analyses

All comparisons were made between animals with the same genetic background, typically littermates, and we used both male and female mice. The number of samples (n) for each comparison can be found in the individual method descriptions and are given in the corresponding figures. Phenotyping and data analysis was performed blind to the genotype of the mice. All values are presented either as the mean ± standard deviation (SD) or standard error of the mean (SEM). For statistical analysis, GraphPad Prism software was used. To assess differences in the mean, one-way or two-way ANOVA with Bonferroni's multiple comparison

test, multiple *t*-tests with Holm-Sidak comparison method, and unpaired two-tailed *t*-tests were employed. Significance was determined as $P < 0.05$ (*), $P < 0.01$ (**), $P < 0.001$ (***) or $P < 0.0001$ (****). Complete results of the statistical analyses are included in the figure legends.

Ethics approval and consent to participate

Experiments were carried out following the animal welfare guidelines 2010/63/EC of the European Communities Council Directive, agreeing with the Guide for the Care and Use of Laboratory Animals (National Research Council. Washington, DC. The National Academies Press, 1996). The design of experiments was approved by the Animal Care and Use Committee of the Institute of Molecular Genetics, Czech Academy of Sciences (protocol # 104/2019).

Consent for publication

Not applicable.

Data availability

All data generated or analyzed during this study are included in this published article, its Additional Supplementary Files 1, 2, and in the publicly available Gene Expression Omnibus (GEO) repository.

Competing interests

The authors declare that they have no competing interests.

Funding

This research was supported by the Czech Science Foundation (20-06927S to GP), by the institutional support of the Czech Academy of Sciences (RVO: 86652036 to GP), and NIH/NIA (R01 AG060504, DC016099, AG051443 to BF and ENY).

Authors' contributions

GP, JS, BF designed and supervised the experiments. IF, KP, RB, MT, SV, MD, and BF performed experiments and analyzed the data. OS, SB, and LV carried RNAseq analyses. IF and KP prepared the first draft of the manuscript. GP and BF wrote the manuscript, ENY and JS reviewed the manuscript. All authors read and approved the final manuscript.

Acknowledgments

A. Pavlinek (King's College London) for editing the MS. We acknowledge Imaging Methods Core Facility at BIOCEV supported by the MEYS CR (Large RI Project LM2018129 Czech-BioImaging) and ERDF (project No. CZ.02.1.01/0.0/0.0/18_046/0016045) for its support with obtaining imaging data presented in this paper and FACS experiments, and Biocev GeneCore Facility for its support with gene expression/transcriptome analyses.

References

1. Muniak MA, Connelly CJ, Suthakar K, Milinkeviciute G, Ayeni FE, Ryugo DK. Central Projections of Spiral Ganglion Neurons. In: *The Primary Auditory Neurons of the Mammalian Cochlea*). Springer (2016).

2. Rubel EW, Fritzsch B. Auditory system development: primary auditory neurons and their targets. *Annu Rev Neurosci* **25**, 51-101 (2002).

3. Kandler K, Clause A, Noh J. Tonotopic reorganization of developing auditory brainstem circuits. *Nat Neurosci* **12**, 711-717 (2009).

4. Di Bonito M, Studer M. Cellular and Molecular Underpinnings of Neuronal Assembly in the Central Auditory System during Mouse Development. *Front Neural Circuits* **11**, 18 (2017).

5. Lopez-Poveda EA. Olivocochlear Efferents in Animals and Humans: From Anatomy to Clinical Relevance. *Front Neurol* **9**, 197 (2018).

6. Fritzsch B, Elliott KL. Evolution and Development of the Inner Ear Efferent System: Transforming a Motor Neuron Population to Connect to the Most Unusual Motor Protein via Ancient Nicotinic Receptors. *Front Cell Neurosci* **11**, 114 (2017).

7. Ma Q, Anderson DJ, Fritzsch B. Neurogenin 1 null mutant ears develop fewer, morphologically normal hair cells in smaller sensory epithelia devoid of innervation. *J Assoc Res Otolaryngol* **1**, 129-143 (2000).

8. Kim W-Y*, et al.* NeuroD-null mice are deaf due to a severe loss of the inner ear sensory neurons during development. *Development* **128**, 417-426 (2001).

9. Duncan JS, Fritzsch B. Continued expression of GATA3 is necessary for cochlear neurosensory development. *PloS one* **8**, e62046 (2013).

10. Appler JM, Lu CC, Druckenbrod NR, Yu WM, Koundakjian EJ, Goodrich LV. Gata3 is a critical regulator of cochlear wiring. *J Neurosci* **33**, 3679-3691 (2013).

11. Huang EJ, Liu W, Fritzsch B, Bianchi LM, Reichardt LF, Xiang M. Brn3a is a transcriptional regulator of soma size, target field innervation and axon pathfinding of inner ear sensory neurons. *Development* **128**, 2421-2432 (2001).

12. Liu M*, et al.* Essential role of BETA2/NeuroD1 in development of the vestibular and auditory systems. *Genes & development* **14**, 2839-2854 (2000).

13. Jahan I, Kersigo J, Pan N, Fritzsch B. Neurod1 regulates survival and formation of connections in mouse ear and brain. *Cell Tissue Res* **341**, 95-110 (2010).

14. Filova I*, et al.* Combined Atoh1 and Neurod1 Deletion Reveals Autonomous Growth of Auditory Nerve Fibers. *Mol Neurobiol* **57**, 5307-5323 (2020).

15. Macova I*, et al.* Neurod1 Is Essential for the Primary Tonotopic Organization and Related Auditory Information Processing in the Midbrain. *J Neurosci* **39**, 984-1004 (2019).

16. Dvorakova M*, et al.* Incomplete and delayed Sox2 deletion defines residual ear neurosensory development and maintenance. *Sci Rep* **6**, 38253 (2016).

17. Radde-Gallwitz K, Pan L, Gan L, Lin X, Segil N, Chen P. Expression of Islet1 marks the sensory and neuronal lineages in the mammalian inner ear. *J Comp Neurol* **477**, 412-421 (2004).

18. Deng M, Yang H, Xie X, Liang G, Gan L. Comparative expression analysis of POU4F1, POU4F2 and ISL1 in developing mouse cochleovestibular ganglion neurons. *Gene Expr Patterns* **15**, 31-37 (2014).

19. Chumak T*, et al.* Overexpression of Isl1 under the Pax2 Promoter, Leads to Impaired Sound Processing and Increased Inhibition in the Inferior Colliculus. *Int J Mol Sci* **22**, (2021).

20. Petitpre C*, et al.* Neuronal heterogeneity and stereotyped connectivity in the auditory afferent system. *Nature communications* **9**, 3691 (2018).

21. Li HJ, Kapoor A, Giel-Moloney M, Rindi G, Leiter AB. Notch signaling differentially regulates the cell fate of early endocrine precursor cells and their maturing descendants in the mouse pancreas and intestine. *Dev Biol* **371**, 156-169 (2012).

22. Sun Y, Dykes IM, Liang X, Eng SR, Evans SM, Turner EE. A central role for Islet1 in sensory neuron development linking sensory and spinal gene regulatory programs. *Nat Neurosci* **11**, 1283-1293 (2008).

23. Jahan I, Pan N, Kersigo J, Fritzsch B. Neurod1 suppresses hair cell differentiation in ear ganglia and regulates hair cell subtype development in the cochlea. *PLoS One* **5**, e11661 (2010).

24. Li C*, et al.* Comprehensive transcriptome analysis of cochlear spiral ganglion neurons at multiple ages. *Elife* **9**, (2020).

25. Stoeckli ET. Understanding axon guidance: are we nearly there yet? *Development* **145**, (2018).

26. Fritzsch B, Kersigo J, Yang T, Jahan I, Pan N. Neurotrophic Factor Function During Ear Development: Expression Changes Define Critical Phases for Neuronal Viability. In: *The Primary Auditory Neurons of the Mammalian Cochlea* (eds Dabdoub A, Fritzsch B, Popper AN, Fay RR). Springer New York (2016).

27. Dennis DJ, Han S, Schuurmans C. bHLH transcription factors in neural development, disease, and reprogramming. *Brain Res* **1705**, 48-65 (2019).

28. Yang T, Kersigo J, Wu S, Fritzsch B, Bassuk AG. Prickle1 regulates neurite outgrowth of apical spiral ganglion neurons but not hair cell polarity in the murine cochlea. *PLoS One* **12**, e0183773 (2017).

29. Bok J, Zenczak C, Hwang CH, Wu DK. Auditory ganglion source of Sonic hedgehog regulates timing of cell cycle exit and differentiation of mammalian cochlear hair cells. *Proc Natl Acad Sci U S A* **110**, 13869-13874 (2013).

30. Shrestha BR, Chia C, Wu L, Kujawa SG, Liberman MC, Goodrich LV. Sensory Neuron Diversity in the Inner Ear Is Shaped by Activity. *Cell* **174**, 1229-1246 e1217 (2018).

31. Pauley S, Wright TJ, Pirvola U, Ornitz D, Beisel K, Fritzsch B. Expression and function of FGF10 in mammalian inner ear development. *Dev Dyn* **227**, 203-215 (2003).

32. Yu Y*, et al.* Sensorineural Hearing Loss and Mitochondrial Apoptosis of Cochlear Spiral Ganglion Neurons in Fibroblast Growth Factor 13 Knockout Mice. *Frontiers in Cellular Neuroscience* **15**, (2021).

33. Fettiplace R, Hackney CM. The sensory and motor roles of auditory hair cells. *Nature reviews Neuroscience* **7**, 19-29 (2006).

34. Neely S, Kim DO. *Cochlear models incorporating active processes*. Springer New York (2007).

35. Muller M, von Hunerbein K, Hoidis S, Smolders JW. A physiological place-frequency map of the cochlea in the CBA/J mouse. *Hear Res* **202**, 63-73 (2005).

36. Zhou X, Jen PH, Seburn KL, Frankel WN, Zheng QY. Auditory brainstem responses in 10 inbred strains of mice. *Brain Res* **1091**, 16-26 (2006).

37. Chambers AR*, et al.* Central Gain Restores Auditory Processing following Near-Complete Cochlear Denervation. *Neuron* **89**, 867-879 (2016).

38. Harris JA, Rubel EW. Afferent regulation of neuron number in the cochlear nucleus: cellular and molecular analyses of a critical period. *Hear Res* **216-217**, 127-137 (2006).

39. Lauer AM, Connelly CJ, Graham H, Ryugo DK. Morphological characterization of bushy cells and their inputs in the laboratory mouse (Mus musculus) anteroventral cochlear nucleus. *PLoS One* **8**, e73308 (2013).

40. Karmakar K*, et al.* Hox2 Genes Are Required for Tonotopic Map Precision and Sound Discrimination in the Mouse Auditory Brainstem. *Cell Rep* **18**, 185-197 (2017).

41. Fujiyama T*, et al.* Inhibitory and excitatory subtypes of cochlear nucleus neurons are defined by distinct bHLH transcription factors, Ptf1a and Atoh1. *Development* **136**, 2049-2058 (2009).

42. Gruters KG, Groh JM. Sounds and beyond: multisensory and other non-auditory signals in the inferior colliculus. *Front Neural Circuits* **6**, 96 (2012).

43. Yeomans JS, Frankland PW. The acoustic startle reflex: neurons and connections. *Brain Research Reviews* **21**, 301-314 (1995).

44. Koch M. The neurobiology of startle. *Progress in neurobiology* **59**, 107-128 (1999).

45. Lee Y, Lopez DE, Meloni EG, Davis M. A primary acoustic startle pathway: obligatory role of cochlear root neurons and the nucleus reticularis pontis caudalis. *J Neurosci* **16**, 3775-3789 (1996).

46. Swerdlow NR, Geyer MA, Braff DL. Neural circuit regulation of prepulse inhibition of startle in the rat: current knowledge and future challenges. *Psychopharmacology* **156**, 194-215 (2001).

47. Fitch RH, Threlkeld SW, McClure MM, Peiffer AM. Use of a modified prepulse inhibition paradigm to assess complex auditory discrimination in rodents. *Brain research bulletin* **76**, 1-7 (2008).

48. Hickox AE, Liberman MC. Is noise-induced cochlear neuropathy key to the generation of hyperacusis or tinnitus? *J Neurophysiol* **111**, 552-564 (2014).

49. Pfaff SL, Mendelsohn M, Stewart CL, Edlund T, Jessell TM. Requirement for LIM homeobox gene Isl1 in motor neuron generation reveals a motor neuron-dependent step in interneuron differentiation. *Cell* **84**, 309-320 (1996).

50. Yang L*, et al.* Isl1Cre reveals a common Bmp pathway in heart and limb development. *Development* **133**, 1575-1585 (2006).

51. Huber K, Narasimhan P, Shtukmaster S, Pfeifer D, Evans SM, Sun Y. The LIM-Homeodomain transcription factor Islet-1 is required for the development of sympathetic neurons and adrenal chromaffin cells. *Dev Biol* **380**, 286-298 (2013).

52. Ahlgren U, Pfaff SL, Jessell TM, Edlund T, Edlund H. Independent requirement for ISL1 in formation of pancreatic mesenchyme and islet cells. *Nature* **385**, 257-260 (1997).

53. Cai CL*, et al.* Isl1 identifies a cardiac progenitor population that proliferates prior to differentiation and contributes a majority of cells to the heart. *Dev Cell* **5**, 877-889 (2003).

54. Liang X*, et al.* Isl1 is required for multiple aspects of motor neuron development. *Molecular and cellular neurosciences* **47**, 215-222 (2011).

55. Kania A, Jessell TM. Topographic motor projections in the limb imposed by LIM homeodomain protein regulation of ephrin-A:EphA interactions. *Neuron* **38**, 581-596 (2003).

56. Yamashita T*, et al.* High-resolution transcriptional dissection of in vivo Atoh1-mediated hair cell conversion in mature cochleae identifies Isl1 as a co-reprogramming factor. *PLoS Genet* **14**, e1007552 (2018).

57. Chumak T*, et al.* Deterioration of the Medial Olivocochlear Efferent System Accelerates Age-Related Hearing Loss in Pax2-Isl1 Transgenic Mice. *Mol Neurobiol* **53**, 2368-2383 (2016).

58. Bohuslavova R*, et al.* Pax2-Islet1 Transgenic Mice Are Hyperactive and Have Altered Cerebellar Foliation. *Mol Neurobiol* **54**, 1352-1368 (2017).

59. Huang M, Kantardzhieva A, Scheffer D, Liberman MC, Chen ZY. Hair cell overexpression of Islet1 reduces age-related and noise-induced hearing loss. *J Neurosci* **33**, 15086-15094 (2013).

60. Morris JK*, et al.* A disorganized innervation of the inner ear persists in the absence of ErbB2. *Brain Res* **1091**, 186-199 (2006).

61. Mao Y, Reiprich S, Wegner M, Fritzsch B. Targeted deletion of Sox10 by Wnt1-cre defects neuronal migration and projection in the mouse inner ear. *PLoS One* **9**, e94580 (2014).

62. Geyer MA, McIlwain KL, Paylor R. Mouse genetic models for prepulse inhibition: an early review. *Mol Psychiatry* **7**, 1039-1053 (2002).

63. LeMasurier M, Gillespie PG. Hair-cell mechanotransduction and cochlear amplification. *Neuron* **48**, 403-415 (2005).

64. Dallos P*, et al.* Prestin-based outer hair cell motility is necessary for mammalian cochlear amplification. *Neuron* **58**, 333-339 (2008).

65. Herranen A*, et al.* Deficiency of the ER-stress-regulator MANF triggers progressive outer hair cell death and hearing loss. *Cell death & disease* **11**, 100 (2020).

66. Liberman LD, Liberman MC. Cochlear Efferent Innervation Is Sparse in Humans and Decreases with Age. *J Neurosci* **39**, 9560-9569 (2019).

67. Hafidi A. Peripherin-like immunoreactivity in type II spiral ganglion cell body and projections. *Brain Res* **805**, 181-190 (1998).

68. Elliott KL*, et al.* Developmental Changes in Peripherin-eGFP Expression in Spiral Ganglion Neurons. *Front Cell Neurosci* **15**, 678113 (2021).

69. Zhang KD, Coate TM. Recent advances in the development and function of type II spiral ganglion neurons in the mammalian inner ear. *Seminars in cell & developmental biology* **65**, 80-87 (2017).

70. Froud KE*, et al.* Type II spiral ganglion afferent neurons drive medial olivocochlear reflex suppression of the cochlear amplifier. *Nature communications* **6**, 7115 (2015).

71. Maison S, Liberman LD, Liberman MC. Type II Cochlear Ganglion Neurons Do Not Drive the Olivocochlear Reflex: Re-Examination of the Cochlear Phenotype in Peripherin Knock-Out Mice. *eNeuro* **3**, (2016).

72. Matei V*, et al.* Smaller inner ear sensory epithelia in Neurog 1 null mice are related to earlier hair cell cycle exit. *Dev Dyn* **234**, 633-650 (2005).

73. Pauley S, Lai E, Fritzsch B. Foxg1 is required for morphogenesis and histogenesis of the mammalian inner ear. *Dev Dyn* **235**, 2470-2482 (2006).

74. Nichols DH, Pauley S, Jahan I, Beisel KW, Millen KJ, Fritzsch B. Lmx1a is required for segregation of sensory epithelia and normal ear histogenesis and morphogenesis. *Cell Tissue Res* **334**, 339-358 (2008).

75. Nichols DH*, et al.* Interaction with ectopic cochlear crista sensory epithelium disrupts basal cochlear sensory epithelium development in Lmx1a mutant mice. *Cell Tissue Res* **380**, 435-448 (2020).

76. Pavlinkova G. Molecular Aspects of the Development and Function of Auditory Neurons. *Int J Mol Sci* **22**, (2020).

77. Zine A, Messat Y, Fritzsch B. A human induced pluripotent stem cell-based modular platform to challenge sensorineural hearing loss. *Stem Cells*, (2021).

78. Hobert O, Westphal H. Functions of LIM-homeobox genes. *Trends Genet* **16**, 75-83 (2000).

79. Mamanova L, Miao Z, Jinat A, Ellis P, Shirley L, Teichmann SA. High-throughput full-length single-cell RNA-seq automation. *Nat Protoc* **16**, 2886-2915 (2021).

80. Dobin A*, et al.* STAR: ultrafast universal RNA-seq aligner. *Bioinformatics* **29**, 15-21 (2013).

81. Martin M. Cutadapt removes adapter sequences from high-throughput sequencing reads. *2011* **17**, 3 (2011).

82. Bolger AM, Lohse M, Usadel B. Trimmomatic: a flexible trimmer for Illumina sequence data. *Bioinformatics* **30**, 2114-2120 (2014).

83. Kopylova E, Noe L, Touzet H. SortMeRNA: fast and accurate filtering of ribosomal RNAs in metatranscriptomic data. *Bioinformatics* **28**, 3211-3217 (2012).

84. Love MI, Huber W, Anders S. Moderated estimation of fold change and dispersion for RNA-seq data with DESeq2. *Genome Biol* **15**, 550 (2014).

85. Boyle EI*, et al.* GO::TermFinder--open source software for accessing Gene Ontology information and finding significantly enriched Gene Ontology terms associated with a list of genes. *Bioinformatics* **20**, 3710-3715 (2004).

86. Raudvere U*, et al.* g:Profiler: a web server for functional enrichment analysis and conversions of gene lists (2019 update). *Nucleic acids research* **47**, W191-W198 (2019).

87. Shannon P*, et al.* Cytoscape: a software environment for integrated models of biomolecular interaction networks. *Genome Res* **13**, 2498-2504 (2003).

88. Merico D, Isserlin R, Stueker O, Emili A, Bader GD. Enrichment map: a network-based method for gene-set enrichment visualization and interpretation. *PLoS One* **5**, e13984 (2010).

89. Fritzsch B, Duncan JS, Kersigo J, Gray B, Elliott KL. Neuroanatomical Tracing Techniques in the Ear: History, State of the Art, and Future Developments. In: *B. Sokolowski, Ed: Auditory and Vestibular Research: Methods and Protocols*). Springer Science+Business Media New York (2016).

90. Simmons D, Duncan J, de Caprona DC, Fritzsch B. Development of the inner ear efferent system. In: *Auditory and vestibular efferents*). Springer (2011).

91. Bures Z, Grécová J, Popelár J, Syka J. Noise exposure during early development impairs the processing of sound intensity in adult rats. *The European journal of neuroscience* **32**, 155-164 (2010).